Article

Modelling and Control of Parallel-Connected Transformerless Inverters for Large Photovoltaic Farms

Marian Liberos *, Raúl González-Medina, Gabriel Garcerá (iD) **and Emilio Figueres**

Grupo de Sistemas Electrónicos Industriales del Departamento de Ingeniería Electrónica, Universitat Politècnica de València, Camino de Vera s/n, 46022 Valencia, Spain; raugonme@upv.es (R.G.-M.); ggarcera@eln.upv.es (G.G.); efiguere@eln.upv.es (E.F.)

* Correspondence: malimas@upv.es; Tel.: +34-963-879-606

Abstract: This paper presents a control structure for transformerless photovoltaic inverters connected in parallel to manage photovoltaic fields in the MW range. Large photovoltaic farms are usually divided into several photovoltaic fields, each one of them managed by a centralized high power inverter. The current tendency to build up centralized inverters in the MW range is the use of several transformerless inverters connected in parallel, a topology that provokes the appearance of significant zero-sequence circulating currents among inverters. To eliminate this inconvenience, this paper proposes a control structure that avoids the appearance of circulating currents by controlling the zero-sequence component of the inverters. A second contribution of the paper is the development of a model of *n* parallel-connected inverters. To validate the concept, the proposed control structure has been applied to a photovoltaic field of 2 MW managed by four 500 kW photovoltaic inverters connected in parallel.

Keywords: photovoltaic farms; parallel inverters; circulating current; modeling and control

1. Introduction

In recent years the demand for electricity has increased. In the future, the global electricity consumption is expected to continue growing significantly [1]. Moreover, the prices of the conventional sources that have a limited stock are increasing, so renewable energies such as the photovoltaic (PV) solar cells are becoming a promising alternative. Photovoltaic energy has many advantages: it is a clean energy, it is omnipresent and has lower operational and maintenance costs [2]. Nowadays, large-scale PV plants that improve the profitability of the photovoltaic systems are proliferating [3].

In the context of photovoltaic fields, there are many studies dealing with the use of decentralized inverters that are connected to only one string with their own Maximum Power Point Tracking (MPPT) [4]. The main benefit of the use of decentralized inverters is the high number of MPPT inputs of these systems. However, decentralized topologies, illustrated in Figure 1a, are less interesting for high power applications because of their high cost. As an alternative, centralized inverters are mostly used in high power applications, because they offer a good compromise between costs and efficiency [5]. Figure 1b–f shows various PV system schemes based on centralized inverters.
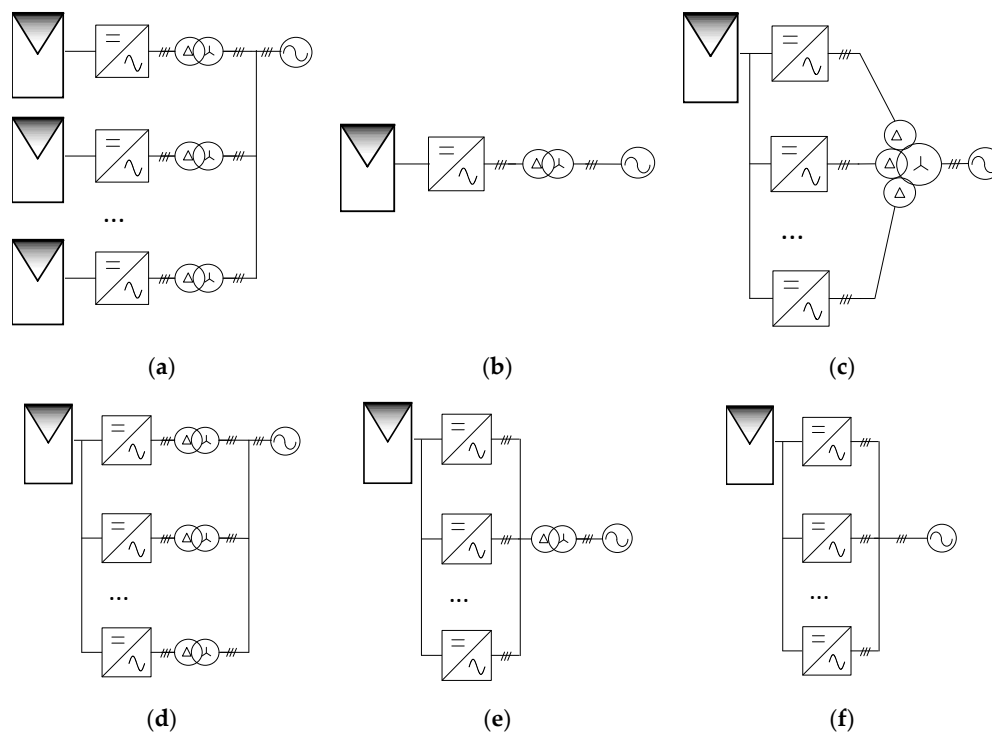
Figure 1. Topologies of high power PV inverters: (**a**) decentralized inverters; (**b**) centralized inverter; (**c**) centralized inverter composed by *n* parallel modules and a multi-output transformer; (**d**) centralized inverter composed by *n* parallel modules and n transformers; (**e**) centralized inverter composed by *n* modules and a single transformer; (**f**) centralized inverter composed by *n* transformerless modules.

Figure 1b illustrates a central inverter that connects the whole PV field to the distribution grid by means of a low frequency transformer. The main problem of using this scheme is the poor efficiency in the low power range, when the radiation conditions are low and the entire system must remain in operation. In addition, the transformer is expensive and bulky. To partially overcome these drawbacks, Figure 1c–f shows several solutions that implement a centralized inverter by means of the parallel connection of modules, each one of them managing a fraction of the full power. The parallel operation of inverters allows modularity and also the inverter disconnection depending on the level of the generated power. This technique is frequently used to improve the efficiency in the low power range, as Figure 3 depicts and will be discussed later. In Figure 1c,d the use of a single multiple-output transformer and an individual transformer per inverter is proposed, respectively. Both solutions take advantage of the paralleling principle, but they are up to 40% more expensive than having a single secondary as in Figure 1e [3]. Although the use of a single transformer for all modules is not as expensive as the two previously described solutions, it is as expensive and bulky as the one of Figure 1b. At this point, the question is whether galvanic isolation is mandatory in photovoltaic installations or if it can be avoided to reduce costs, volume and weight, as well as power losses of the system. It is true that transformers allow filtering out the DC components of the generated currents, so that these components are not injected to the distribution grid, as it is stated by standards and regulations about the grid connection of power inverters. However, for this purpose the use of transformers can be replaced by any technique that limits the generated DC components below a certain threshold that would depend on the local regulations of each country. This fact opens the way to the use of transformerless inverters in PV installations, which are much less bulky and expensive and also avoid the power losses produced by transformers. To illustrate this fact, Figure 2 shows the efficiency of the Power Gate Plus 500 kW, a high power inverter manufactured by Satcon (Shiyan, China). In this figure the efficiency in the whole power range with (in red) and without transformer (in green) has been

represented according to the datasheet [6]. It can be noted that the efficiency of the transformerless version of the inverter is significantly greater in the whole power range.
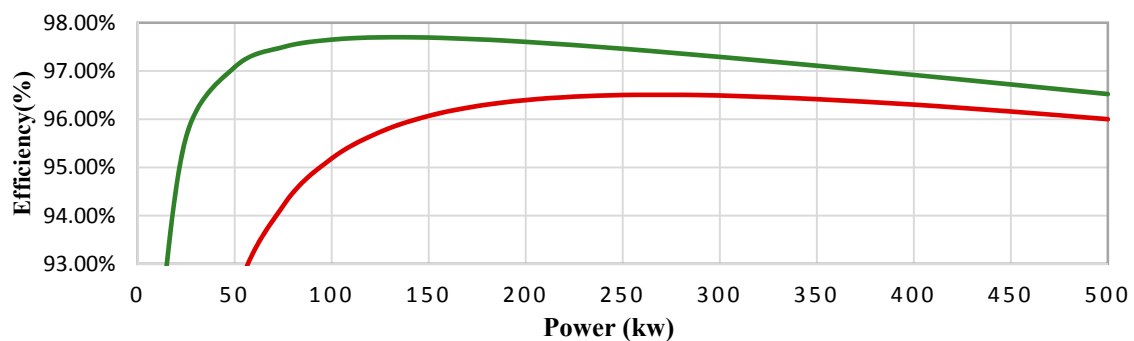

Figure 2. Efficiency of the Power Gate Plus 500 kW from Satcon with (in red) and without transformer (in green).

This work focuses on the parallel connection of *n* transformerless inverters as Figure 1f shows. As stated above, this connection has many benefits such as modularity, better profitability and lower volume, weight and costs. The efficiency of a centralized inverter constituted by a single module that manages all the power is poor when the generated power is low. As a solution to this problem, topologies composed of inverters connected in parallel are usually employed [7–9]. The main benefit of these systems is that each inverter can be connected as the generated power increases. To illustrate this fact, Figure 3 illustrates the efficiency considering a single inverter which manages the full power (in red), and the efficiency of four parallel inverters managing each one a fraction of the total power (in blue). The improvement of the efficiency is evident at the low power range, in which the inverters work for many hours. Note that the inverters can be sequentially connected to achieve the better efficiency profile in the whole range of power, as Figure 3 shows. The data to build up the efficiency profiles have been obtained from [6]. It is worth to point out that there are companies that manufacture photovoltaic inverters in the MW range. To achieve this power range, several modules of around 500 kW are usually connected in parallel, as it is the case of the HEC V1000 (Power Electronics, Paterna, Valencia) [8] and the VS980 solar inverter (ABB, Zürich, Switzerland) [9]. The switches market currently offers a large variety of stacks that could be used in these applications. For instance, the company Infineon (Neubiberg, Germany) has the PrimePACK$^{\text{TM}}$ Module series up to 1700 V-1400 A, which are recommended for 2-level topologies [10].
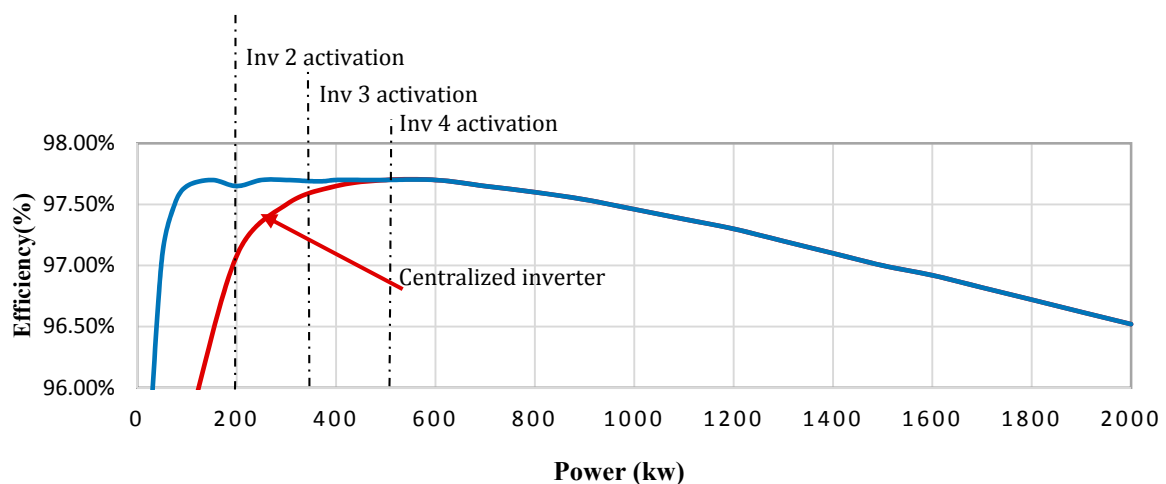

Figure 3. Efficiency of a single inverter (red) vs several parallel-connected inverters (blue).

In spite of their advantages, the main problem of connecting parallel inverters is the appearance of circulating currents that have a zero-sequence nature. In parallel operation, the converters are usually designed individually, but when they operate in parallel, a zero-sequence circulating current that can produce malfunctions in the system appears [11]. To overcome this problem, in [12–14], it was proposed the use of isolating transformers as in Figure 1c,d, but therefore an expensive and bulky system results. In other works [15,16], the *n* parallel modules are treated as only one by considering an equivalent single converter that has as many legs as the number of legs of each module multiplied by *n*. Nevertheless, this approach doesn't allow modular design and has a great degree of complexity, so that it is only suitable for low values of *n*.

In this paper a control technique that eliminates the problem of circulating currents by controlling the zero-sequence components of the generated currents is proposed. To achieve this, the proposed technique implements a three-dimension space vector modulator into the control loop of $n-1$ inverters. The complexity of the proposed solution is very low and, as it will be shown in the next sections, it is compatible with modular design and can be easily extended to high values of *n*. Another contribution of the paper is the development of an accurate model of these kinds of PV systems.

2. Modeling of *n* Parallel pv Inverters in a Synchronous Reference Frame

Figure 4 depicts the scheme of *n* PV transformerless inverters connected in parallel. The grid filter for each inverter is an LCL network that has damping resistors, R_d, connected in series to the filter capacitors. In the model of the system the mutual coupling terms, M_a and M_b, of the three-phase inductors, L_a and L_b, have been taken into account. It is worth to point out that the coupling terms are usually neglected, even if three-phase inductors instead of one inductor per phase are used. However, they affect to the dynamic response of the system, so that it is interesting to consider them. In the model, the grid inductance L_g has been also considered.
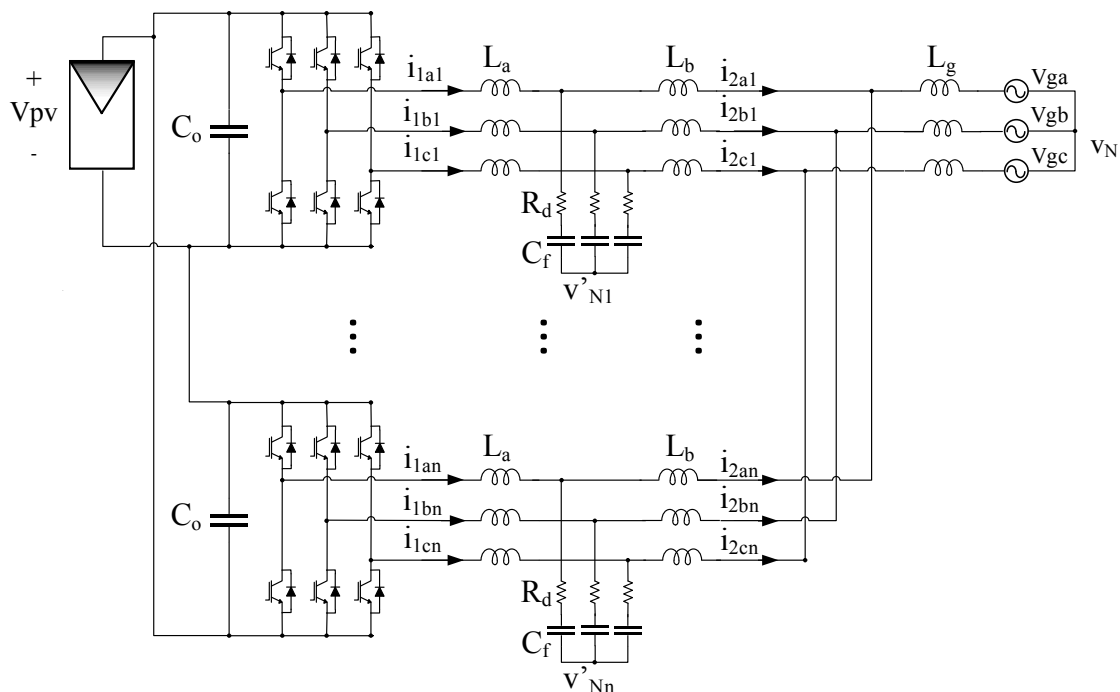

Figure 4. Scheme of *n* PV transformerless inverters connected in parallel with LCL grid filters.

2.1. Equations of the Averaged Model

Figure 5c shows the equivalent circuit of only one inverter leg, which is derived by averaging in a switching cycle the grid voltage and the DC current that appear in Figure 5a. In Figure 5b the

instantaneous and averaged values of the variables are represented, being d_ϕ, ($\phi = a$, b, and c) the duty cycle of the upper Insulated Gate Bipolar Transistor (IGBT) (i.e., of the control signal $S_{\phi p}$).

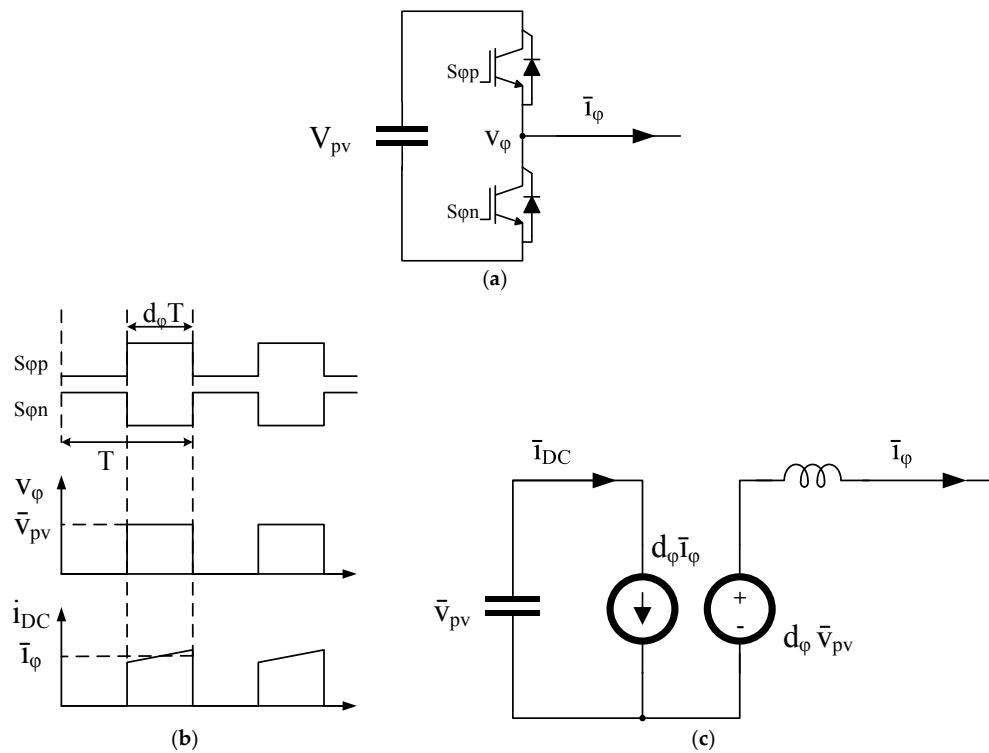**Figure 5.** Averaged equivalent circuit of an inverter leg: (**a**) Inverter leg; (**b**) Switching time and relationship among input and output variables; (**c**) Averaged equivalent circuit.

By applying the averaged equivalent circuit to each one of the inverter legs in Figure 4, the averaged model of the *n* parallel transformerless PV inverters in the stationary three-phase frame is obtained, as Figure 6 shows. Equations (1)–(8) are directly obtained from this scheme. In the equations, $i = 1, \ldots, n$ identifies each one of the modules and *n* is the total number of modules. Note that Equations (5)–(7) are equal for each inverter if the components are considered of the same value and if tolerances around the nominal values are neglected.
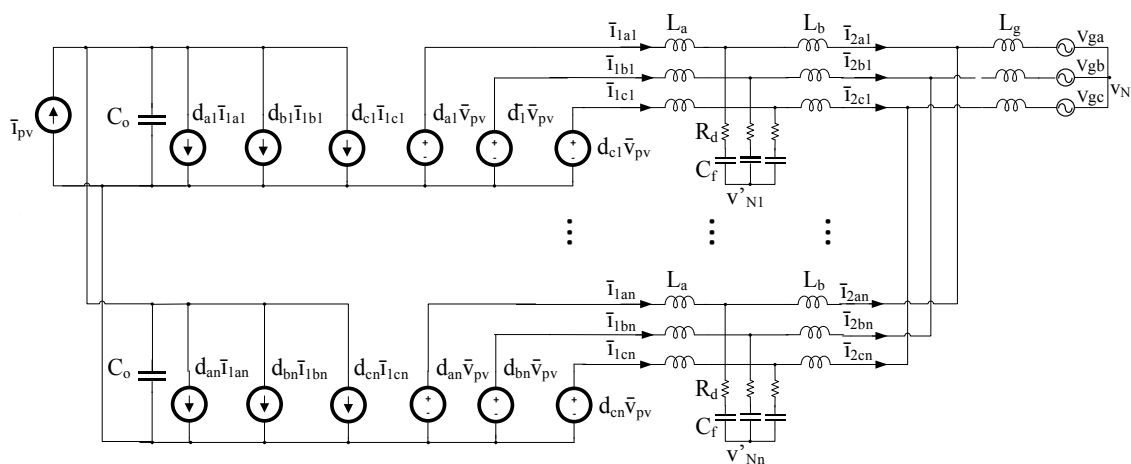

Figure 6. Averaged equivalent circuit of *n* PV transformerless inverters connected in parallel.

$$V_{L_a i} = L_a \cdot \frac{d}{dt}\bar{i}_{1ai} + M_a \cdot \frac{d}{dt}\bar{i}_{1bi} + M_a \cdot \frac{d}{dt}\bar{i}_{1ci} \tag{1}$$

$$V_{L_b i} = M_a \cdot \frac{d}{dt}\bar{i}_{1ai} + L_a \cdot \frac{d}{dt}\bar{i}_{1bi} + M_a \cdot \frac{d}{dt}\bar{i}_{1ci} \tag{2}$$

$$V_{L_c i} = M_a \cdot \frac{d}{dt}\bar{i}_{1ai} + M_a \cdot \frac{d}{dt}\bar{i}_{1bi} + L_a \cdot \frac{d}{dt}\bar{i}_{1ci} \tag{3}$$

$$\bar{i}_{g\varphi} = \bar{i}_{2\varphi 1} + \bar{i}_{2\varphi 2} + \ldots + \bar{i}_{2\varphi n} = n\bar{i}_{2\varphi} \tag{4}$$

$$\begin{bmatrix} L_a & M_a & M_a \\ M_a & L_a & M_a \\ M_a & M_a & L_a \end{bmatrix} \frac{d}{dt} \begin{bmatrix} \bar{i}_{1ai} \\ \bar{i}_{1bi} \\ \bar{i}_{1ci} \end{bmatrix} = \bar{v}_{pv} \begin{bmatrix} \bar{d}_{ai} \\ \bar{d}_{bi} \\ \bar{d}_{ci} \end{bmatrix} - \begin{bmatrix} \bar{v}_{cai} \\ \bar{v}_{cbi} \\ \bar{v}_{cci} \end{bmatrix} - R_d \begin{bmatrix} \bar{i}_{1ai} \\ \bar{i}_{1bi} \\ \bar{i}_{1ci} \end{bmatrix} + R_d \begin{bmatrix} \bar{i}_{2ai} \\ \bar{i}_{2bi} \\ \bar{i}_{2ci} \end{bmatrix} - \begin{bmatrix} \bar{v}_{N'} \\ \bar{v}_{N'} \\ \bar{v}_{N'} \end{bmatrix} \tag{5}$$

$$\begin{bmatrix} L_b + nL_g & M_b & M_b \\ M_b & L_b + nL_g & M_b \\ M_b & M_b & L_b n + L_g \end{bmatrix} \frac{d}{dt} \begin{bmatrix} \bar{i}_{2ai} \\ \bar{i}_{2bi} \\ \bar{i}_{2ci} \end{bmatrix} = \begin{bmatrix} \bar{v}_{N'} \\ \bar{v}_{N'} \\ \bar{v}_{N'} \end{bmatrix} + \begin{bmatrix} \bar{v}_{cai} \\ \bar{v}_{cbi} \\ \bar{v}_{cci} \end{bmatrix} + R_d \begin{bmatrix} \bar{i}_{1ai} \\ \bar{i}_{1bi} \\ \bar{i}_{1ci} \end{bmatrix} - R_d \begin{bmatrix} \bar{i}_{2ai} \\ \bar{i}_{2bi} \\ \bar{i}_{2ci} \end{bmatrix} - \begin{bmatrix} \bar{v}_{ga} \\ \bar{v}_{gb} \\ \bar{v}_{gc} \end{bmatrix} - \begin{bmatrix} \bar{v}_{N} \\ \bar{v}_{N} \\ \bar{v}_{N} \end{bmatrix} \tag{6}$$

$$\frac{d}{dt} \begin{bmatrix} \bar{v}_{cai} \\ \bar{v}_{cbi} \\ \bar{v}_{cci} \end{bmatrix} = \frac{1}{C_f} \left(\begin{bmatrix} \bar{i}_{1ai} \\ \bar{i}_{1bi} \\ \bar{i}_{1ci} \end{bmatrix} - \begin{bmatrix} \bar{i}_{2ai} \\ \bar{i}_{2bi} \\ \bar{i}_{2ci} \end{bmatrix} \right) \tag{7}$$

$$\frac{d}{dt}\bar{v}_{pv} = \frac{1}{nC_o} \left(\bar{l}_{pv} - \begin{bmatrix} \bar{d}_{a1} \\ \bar{d}_{b1} \\ \bar{d}_{c1} \end{bmatrix}^T \cdot \begin{bmatrix} \bar{i}_{1a1} \\ \bar{i}_{1b1} \\ \bar{i}_{1c1} \end{bmatrix} - \begin{bmatrix} \bar{d}_{a2} \\ \bar{d}_{b2} \\ \bar{d}_{c2} \end{bmatrix}^T \cdot \begin{bmatrix} \bar{i}_{1a2} \\ \bar{i}_{1b2} \\ \bar{i}_{1c2} \end{bmatrix} - \cdots - \begin{bmatrix} \bar{d}_{an} \\ \bar{d}_{bn} \\ \bar{d}_{cn} \end{bmatrix}^T \cdot \begin{bmatrix} \bar{i}_{1an} \\ \bar{i}_{1bn} \\ \bar{i}_{1cn} \end{bmatrix} \right) \tag{8}$$

As it was mentioned above, the mutual coupling terms of the three-phase inductors have been taken into account. Equations (1)–(3) indicate the voltage of the inductor in the phase *a*, *b* and *c*, respectively, in the inverter side of the LCL filter. Similar equations represent the voltage of the three-phase inductor in the grid side of the inverter. In addition, the currents of all the inverters are equal, as expressed by (4), because this will be one of the goals of the control stage.

The PV system has been modelled in a synchronous reference frame (SRF) in which the grid voltage is aligned with the *d*-axis. This approach allows independent control of the active power with the *d*-channel current, while the reactive power is controlled with the *q*-channel current. Regulating the *o*-channel current, which represents the zero-sequence component, it may be controlled the circulating current. The equations of the system in the SRF (11)–(14) have been obtained after multiplying Equations (5)–(8) by the SRF transformation matrix (9) and applying (10) (Park Transformation), following a similar procedure to the one described in [17]. In these equations ω denotes the grid angular frequency and *x* represents any of the average variables. The auxiliary terms K_a, K_b, I_{L_a} and I_{L_b} are defined by (15)–(18). It is worth noting that, in [17], a single three-phase three-wire inverter was studied. In such conditions, the zero-sequence component is null and it was omitted. In addition, independent inductors (one per phase) were considered, so they are no coupling terms among them:

$$T = \sqrt{\frac{2}{3}} \begin{bmatrix} \cos\omega t & \cos\left(\omega t - \frac{2\pi}{3}\right) & \cos\left(\omega t + \frac{2\pi}{3}\right) \\ -\sin\omega t & -\sin\left(\omega t - \frac{2\pi}{3}\right) & -\sin\left(\omega t + \frac{2\pi}{3}\right) \\ \frac{1}{\sqrt{2}} & \frac{1}{\sqrt{2}} & \frac{1}{\sqrt{2}} \end{bmatrix} \tag{9}$$

$$\begin{bmatrix} \bar{x}_d \\ \bar{x}_q \\ \bar{x}_o \end{bmatrix} = T \cdot \begin{bmatrix} \bar{x}_a \\ \bar{x}_b \\ \bar{x}_c \end{bmatrix} \leftrightarrow \begin{bmatrix} \bar{x}_a \\ \bar{x}_b \\ \bar{x}_c \end{bmatrix} = T^{-1} \begin{bmatrix} \bar{x}_d \\ \bar{x}_q \\ \bar{x}_o \end{bmatrix} \tag{10}$$

$$\frac{d}{dt}\begin{bmatrix} \bar{i}_{1di} \\ \bar{i}_{1qi} \\ \bar{i}_{1oi} \end{bmatrix} = -T\frac{dT^{-1}}{dt}\begin{bmatrix} \bar{i}_{1di} \\ \bar{i}_{1qi} \\ \bar{i}_{1oi} \end{bmatrix} + \bar{v}_{pv}I_{L_a}\begin{bmatrix} \bar{d}_{di} \\ \bar{d}_{qi} \\ \bar{d}_{oi} \end{bmatrix} - I_{L_a}\begin{bmatrix} \bar{v}_{cdi} \\ \bar{v}_{cqi} \\ \bar{v}_{coi} \end{bmatrix}$$

$$-R_d I_{L_a}\begin{bmatrix} \bar{i}_{1di} \\ \bar{i}_{1qi} \\ \bar{i}_{1oi} \end{bmatrix} + R_d I_{L_a}\begin{bmatrix} \bar{i}_{2di} \\ \bar{i}_{2qi} \\ \bar{i}_{2oi} \end{bmatrix} - \sqrt{3}\bar{v}_{N'}I_{L_a}\begin{bmatrix} 0 \\ 0 \\ 1 \end{bmatrix} \tag{11}$$

$$\frac{d}{dt}\begin{bmatrix} \bar{i}_{2di} \\ \bar{i}_{2qi} \\ \bar{i}_{2oi} \end{bmatrix} = -T\frac{dT^{-1}}{dt}\begin{bmatrix} \bar{i}_{2di} \\ \bar{i}_{2qi} \\ \bar{i}_{2oi} \end{bmatrix} + I_{L_b}\begin{bmatrix} \bar{v}_{cdi} \\ \bar{v}_{cqi} \\ \bar{v}_{coi} \end{bmatrix} + R_d I_{L_b}\begin{bmatrix} \bar{i}_{1di} \\ \bar{i}_{1qi} \\ \bar{i}_{1oi} \end{bmatrix} - R_d I_{L_b}\begin{bmatrix} \bar{i}_{2di} \\ \bar{i}_{2qi} \\ \bar{i}_{2oi} \end{bmatrix}$$

$$-I_{L_b}\begin{bmatrix} \bar{v}_{gd} \\ \bar{v}_{gq} \\ \bar{v}_{go} \end{bmatrix} - \sqrt{3}(\bar{v}_{N'} - \bar{v}_N)I_{L_b}\begin{bmatrix} 0 \\ 0 \\ 1 \end{bmatrix} \tag{12}$$

$$\frac{d}{dt}\begin{bmatrix} \bar{v}_{cdi} \\ \bar{v}_{cqi} \\ \bar{v}_{coi} \end{bmatrix} = -T\frac{dT^{-1}}{dt}\begin{bmatrix} \bar{i}_{2di} \\ \bar{i}_{2qi} \\ \bar{i}_{2oi} \end{bmatrix} + \frac{1}{C_f}\left(\begin{bmatrix} \bar{i}_{1di} \\ \bar{i}_{1qi} \\ \bar{i}_{1oi} \end{bmatrix} - \begin{bmatrix} \bar{i}_{2di} \\ \bar{i}_{2qi} \\ \bar{i}_{2oi} \end{bmatrix}\right) \tag{13}$$

$$\frac{d}{dt}\bar{v}_{pv} = \frac{1}{nC_o}\left(\bar{l}_{pv} - \left(T^{-1}\begin{bmatrix} \bar{d}_{d1} \\ \bar{d}_{q1} \\ \bar{d}_{o1} \end{bmatrix}\right)^T \cdot T^{-1}\begin{bmatrix} \bar{i}_{1d1} \\ \bar{i}_{1q1} \\ \bar{i}_{1c1} \end{bmatrix} - \left(T^{-1}\begin{bmatrix} \bar{d}_{d2} \\ \bar{d}_{q2} \\ \bar{d}_{o2} \end{bmatrix}\right)^T \cdot T^{-1}\begin{bmatrix} \bar{i}_{1d2} \\ \bar{i}_{1q2} \\ \bar{i}_{1o2} \end{bmatrix}\right.$$

$$\left. - \ldots - \left(T^{-1}\begin{bmatrix} \bar{d}_{dn} \\ \bar{d}_{qn} \\ \bar{d}_{on} \end{bmatrix}\right)^T \cdot T^{-1}\begin{bmatrix} \bar{i}_{1dn} \\ \bar{i}_{1qn} \\ \bar{i}_{1on} \end{bmatrix}\right) \tag{14}$$

$$K_a = (L_a + 2M_a)(L_a - M_a) \tag{15}$$

$$K_b = (L_b + nL_g + 2M_b)(L_b + nL_g - M_b) \tag{16}$$

$$I_{L_a} = \begin{bmatrix} \frac{L_a + M_a}{K_a} & -\frac{M_a}{K_a} & -\frac{M_a}{K_a} \\ -\frac{M_a}{K_a} & \frac{L_a + M_a}{K_a} & -\frac{M_a}{K_a} \\ -\frac{M_a}{K_a} & -\frac{M_a}{K_a} & \frac{L_a + M_a}{K_a} \end{bmatrix} \tag{17}$$

$$I_{L_b} = \begin{bmatrix} \frac{L_b + nL_g + M_b}{K_b} & -\frac{M_b}{K_b} & -\frac{M_b}{K_b} \\ -\frac{M_b}{K_b} & \frac{L_b + nL_g + M_b}{K_b} & -\frac{M_b}{K_b} \\ -\frac{M_b}{K_b} & -\frac{M_b}{K_b} & \frac{L_b + nL_g + M_b}{K_b} \end{bmatrix} \tag{18}$$

Taking into account (19) and (20) and solving, the equations of the average model in the SRF are obtained, following (21)–(24):

$$T\frac{dT^{-1}}{dt} = \begin{bmatrix} 0 & -\omega & 0 \\ \omega & 0 & 0 \\ 0 & 0 & 0 \end{bmatrix} \tag{19}$$

$$\left(A^{-1}B\right)^T A^{-1} = B^T\left(A^{-1}\right)^T A^{-1} = B^T \tag{20}$$

$$\frac{d}{dt}\begin{bmatrix} \bar{i}_{1di} \\ \bar{v}_{1qi} \\ \bar{v}_{1oi} \end{bmatrix} = -\begin{bmatrix} 0 & -\omega & 0 \\ \omega & 0 & 0 \\ 0 & 0 & 0 \end{bmatrix}\begin{bmatrix} \bar{i}_{1di} \\ \bar{i}_{1qi} \\ \bar{i}_{1oi} \end{bmatrix} + \bar{v}_{pv}I_{L_a}\begin{bmatrix} \bar{d}_{di} \\ \bar{d}_{qi} \\ \bar{d}_{oi} \end{bmatrix} - I_{L_a}\begin{bmatrix} \bar{v}_{cdi} \\ \bar{v}_{cqi} \\ \bar{v}_{coi} \end{bmatrix}$$

$$-R_d I_{L_a}\begin{bmatrix} \bar{i}_{1di} \\ \bar{i}_{1qi} \\ \bar{i}_{1oi} \end{bmatrix} + R_d I_{L_a}\begin{bmatrix} \bar{i}_{2di} \\ \bar{i}_{2qi} \\ \bar{i}_{2oi} \end{bmatrix} - \sqrt{3}\bar{v}_{N'}I_{L_a}\begin{bmatrix} 0 \\ 0 \\ 1 \end{bmatrix} \tag{21}$$

$$\frac{d}{dt}\begin{bmatrix} \bar{i}_{2di} \\ \bar{v}_{2qi} \\ \bar{v}_{2oi} \end{bmatrix} = -\begin{bmatrix} 0 & -\omega & 0 \\ \omega & 0 & 0 \\ 0 & 0 & 0 \end{bmatrix}\begin{bmatrix} \bar{i}_{2di} \\ \bar{i}_{2qi} \\ \bar{i}_{2oi} \end{bmatrix} + I_{L_b}\begin{bmatrix} \bar{v}_{cdi} \\ \bar{v}_{cqi} \\ \bar{v}_{coi} \end{bmatrix} + R_d I_{L_b}\begin{bmatrix} \bar{i}_{1di} \\ \bar{v}_{1qi} \\ \bar{v}_{1oi} \end{bmatrix}$$

$$-R_d I_{L_b}\begin{bmatrix} \bar{i}_{2di} \\ \bar{v}_{2qi} \\ \bar{v}_{2oi} \end{bmatrix} - I_{L_b}\begin{bmatrix} \bar{v}_{gd} \\ \bar{v}_{gq} \\ \bar{v}_{go} \end{bmatrix} - \sqrt{3}(\bar{v}_{N'} - \bar{v}_N)I_{L_b}\begin{bmatrix} 0 \\ 0 \\ 1 \end{bmatrix} \tag{22}$$

$$\frac{d}{dt}\begin{bmatrix} \bar{v}_{cdi} \\ \bar{v}_{cqi} \\ \bar{v}_{coi} \end{bmatrix} = -\begin{bmatrix} 0 & -\omega & 0 \\ \omega & 0 & 0 \\ 0 & 0 & 0 \end{bmatrix}\begin{bmatrix} \bar{i}_{2di} \\ \bar{i}_{2qi} \\ \bar{i}_{2oi} \end{bmatrix} + \frac{1}{C_f}\left(\begin{bmatrix} \bar{i}_{1di} \\ \bar{i}_{1qi} \\ \bar{i}_{1oi} \end{bmatrix} - \begin{bmatrix} \bar{i}_{2di} \\ \bar{i}_{2qi} \\ \bar{i}_{2oi} \end{bmatrix}\right) \tag{23}$$

$$\frac{d}{dt}\bar{v}_{pv} = \frac{1}{nC_o}\left(\bar{i}_{pv} - \begin{bmatrix} \bar{d}_{d1} \\ \bar{d}_{q1} \\ \bar{d}_{o1} \end{bmatrix}^T \cdot \begin{bmatrix} \bar{i}_{1d1} \\ \bar{i}_{1q1} \\ \bar{i}_{1c1} \end{bmatrix} - \begin{bmatrix} \bar{d}_{d2} \\ \bar{d}_{q2} \\ \bar{d}_{o2} \end{bmatrix}^T \cdot \begin{bmatrix} \bar{i}_{1d2} \\ \bar{i}_{1q2} \\ \bar{i}_{1o2} \end{bmatrix} - \ldots - \begin{bmatrix} \bar{d}_{dn} \\ \bar{d}_{qn} \\ \bar{d}_{on} \end{bmatrix}^T \cdot \begin{bmatrix} \bar{i}_{1dn} \\ \bar{i}_{1qn} \\ \bar{i}_{1on} \end{bmatrix}\right) \tag{24}$$

2.2. Development of the Small-Signal Model in the State Space

The small-signal equations of the system are obtained by perturbing the average variables around an operating point. In Equation (25), $\bar{x}$ represents each one of the variables of the averaged model, X is the operating point and $\hat{x}$ is the small-signal value of the variable x. After applying (25) to the SRF Equations (21)–(24), the small signal equations of the model in the SRF frame have been obtained, following (26)–(33). Note that the model is quite complex, so that some auxiliary matrices (34)–(43) have been defined to simplify the expressions of A, B, C and D. Note that the input vector U contains both control variables (the duty cycles of each inverter leg) and disturbances (the d and the q terms of the grid voltage):

$$\bar{x} = X + \hat{x} \tag{25}$$

$$\frac{d}{dt}X = A \cdot X + B \cdot U \tag{26}$$

$$Y = C \cdot X + D \cdot U \tag{27}$$

$$X = Y = \begin{bmatrix} \hat{i}_{1d1} & \hat{i}_{1q1} & \hat{i}_{1o1} & \hat{i}_{2d1} & \hat{i}_{2q1} & \hat{i}_{2o1} & \cdots & \hat{i}_{1dn} & \hat{i}_{1qn} & \hat{i}_{1on} & \hat{i}_{2dn} & \hat{i}_{2qn} & \hat{i}_{2on} \\ & \cdots & \cdots & \hat{v}_{cd1} & \hat{v}_{cq1} & \hat{v}_{co1} & \cdots & \hat{v}_{cdn} & \hat{v}_{cqn} & \hat{v}_{con} & \hat{v}_{pv} \end{bmatrix}^T \tag{28}$$

$$U = \begin{bmatrix} \hat{d}_{d1} & \hat{d}_{q1} & \hat{d}_{o1} & \cdots & \hat{d}_{dn} & \hat{d}_{qn} & \hat{d}_{on} & \hat{v}_{gd} & \hat{v}_{gq} & \hat{v}_{go} \end{bmatrix}^T \tag{29}$$

$$
A = \begin{bmatrix}
A_{11} & 0 & \cdots & 0 & A_{21} & 0 & \cdots & 0 & A_{31} \\
0 & A_{12} & \cdots & 0 & 0 & A_{22} & \cdots & 0 & A_{32} \\
\vdots & \vdots & \ddots & \vdots & \vdots & \vdots & \ddots & \vdots & \vdots \\
0 & 0 & \cdots & A_{1n} & 0 & 0 & \cdots & A_{2n} & A_{3n} \\
A_{41} & 0 & \cdots & 0 & A_{51} & 0 & \cdots & 0 & 0 \\
0 & A_{42} & \cdots & 0 & 0 & A_{52} & \cdots & 0 & 0 \\
\vdots & \vdots & \ddots & \vdots & \vdots & \vdots & \ddots & \vdots & \vdots \\
0 & 0 & \cdots & A_{4n} & 0 & 0 & \cdots & A_{5n} & 0 \\
A_{61} & A_{62} & \cdots & A_{6n} & 0 & 0 & \cdots & 0 & \frac{-K_{pv}}{nC_o}
\end{bmatrix}
\tag{30}
$$

$$
B = \begin{bmatrix}
B_{11} & 0 & \cdots & 0 & B_{21} \\
0 & B_{12} & \cdots & 0 & B_{22} \\
\vdots & \vdots & \ddots & \vdots & \vdots \\
0 & 0 & \cdots & B_{1n} & B_{2n} \\
0 & 0 & \cdots & 0 & 0 \\
0 & 0 & \cdots & 0 & 0 \\
\vdots & \vdots & \ddots & \vdots & \vdots \\
0 & 0 & \cdots & 0 & 0 \\
B_{31} & B_{32} & \cdots & B_{3n} & 0
\end{bmatrix}
\tag{31}
$$

$$
C = I \tag{32}
$$

$$
D = 0 \tag{33}
$$

$$
A_{1i} = \begin{bmatrix}
-\frac{R_d(L_a+M_a)}{K_a} & \omega+\frac{R_dM_a}{K_a} & \frac{R_dM_a}{K_a} & \frac{R_d(L_a+M_a)}{K_a} & -\frac{R_dM_a}{K_a} & -\frac{R_dM_a}{K_a} \\
-\omega+\frac{R_dM_a}{K_a} & -\frac{R_d(L_a+M_a)}{K_a} & \frac{R_dM_a}{K_a} & -\frac{R_dM_a}{K_a} & \frac{R_d(L_a+M_a)}{K_a} & -\frac{R_dM_a}{K_a} \\
\frac{R_dM_a}{K_a} & \frac{R_dM_a}{K_a} & -\frac{R_d(L_a+M_a)}{K_a} & -\frac{R_dM_a}{K_a} & -\frac{R_dM_a}{K_a} & \frac{R_d(L_a+M_a)}{K_a} \\
\frac{R_d(L_b+nL_g+M_b)}{K_b} & -\frac{R_dM_b}{K_b} & -\frac{R_dM_b}{K_b} & -\frac{R_d(L_b+nL_g+M_b)}{K_b} & \omega+\frac{R_dM_b}{K_b} & \frac{R_dM_b}{K_b} \\
-\frac{R_dM_b}{K_b} & \frac{R_d(L_b+nL_g+M_b)}{K_b} & -\frac{R_dM_b}{K_b} & -\omega+\frac{R_dM_b}{K_b} & -\frac{R_d(L_b+nL_g+M_b)}{K_b} & \frac{R_dM_b}{K_b} \\
-\frac{R_dM_b}{K_b} & -\frac{R_dM_b}{K_b} & \frac{R_d(L_b+nL_g+M_b)}{K_b} & \frac{R_dM_b}{K_b} & \frac{R_dM_b}{K_b} & -\frac{R_d(L_b+nL_g+M_b)}{K_b}
\end{bmatrix}
\tag{34}
$$

$$
A_{2i} = \begin{bmatrix}
-\frac{L_a+M_a}{K_a} & \frac{M_a}{K_a} & \frac{M_a}{K_a} \\
\frac{M_a}{K_a} & -\frac{L_a+M_a}{K_a} & \frac{M_a}{K_a} \\
\frac{M_a}{K_a} & \frac{M_a}{K_a} & -\frac{L_a+M_a}{K_a} \\
\frac{L_b+nL_g+M_b}{K_b} & -\frac{M_b}{K_b} & -\frac{M_b}{K_b} \\
-\frac{M_b}{K_b} & \frac{L_b+nL_g+M_b}{K_b} & -\frac{M_b}{K_b} \\
-\frac{M_b}{K_b} & -\frac{M_b}{K_b} & \frac{L_b+nL_g+M_b}{K_b}
\end{bmatrix}
\tag{35}
$$

$$
A_{3i} = \begin{bmatrix}
\frac{D_d(L_a+M_a)-D_qM_a-D_oM_a}{K_a} \\
\frac{-D_dM_a+D_q(L_a+M_a)-D_oM_a}{K_a} \\
\frac{D_dM_a-D_qM_a+D_oM_a}{K_a} \\
0 \\
0 \\
0
\end{bmatrix}
\tag{36}
$$

$$A_{4i} = \begin{bmatrix} \frac{1}{C_f} & 0 & 0 & -\frac{1}{C_f} & 0 & 0 \\ 0 & \frac{1}{C_f} & 0 & 0 & -\frac{1}{C_f} & 0 \\ 0 & 0 & \frac{1}{C_f} & 0 & 0 & -\frac{1}{C_f} \end{bmatrix} \tag{37}$$

$$A_{5i} = \begin{bmatrix} 0 & \omega & 0 \\ -\omega & 0 & 0 \\ 0 & 0 & 0 \end{bmatrix} \tag{38}$$

$$A_{6i} = \begin{bmatrix} -\frac{D_d}{nC_o} & -\frac{D_q}{nC_o} & -\frac{D_o - D_o}{nC_o} & 0 & 0 & 0 \end{bmatrix} \tag{39}$$

$$B_{1i} = \begin{bmatrix} \frac{V_{pv}(L_a + M_a)}{K_a} & -\frac{V_{pv}M_a}{K_a} & -\frac{V_{pv}M_a}{K_a} \\ -\frac{V_{pv}M_a}{K_a} & \frac{V_{pv}(L_a + M_a)}{K_a} & -\frac{V_{pv}M_a}{K_a} \\ -\frac{V_{pv}M_a}{K_a} & -\frac{V_{pv}M_a}{K_a} & \frac{V_{pv}(L_a + M_a)}{K_a} \\ 0 & 0 & 0 \\ 0 & 0 & 0 \\ 0 & 0 & 0 \end{bmatrix} \tag{40}$$

$$B_{2i} = \begin{bmatrix} 0 & 0 & 0 \\ 0 & 0 & 0 \\ 0 & 0 & 0 \\ -\frac{L_b + nL_g + M_b}{K_b} & \frac{M_b}{K_b} & \frac{M_b}{K_b} \\ \frac{M_b}{K_b} & -\frac{L_b + nL_g + M_b}{K_b} & \frac{M_b}{K_b} \\ \frac{M_b}{K_b} & \frac{M_b}{K_b} & -\frac{L_b + nL_g + M_b}{K_b} \end{bmatrix} \tag{41}$$

$$B_{31,2,\ \dots,n-1} = \begin{bmatrix} -\frac{I_d}{nC_o} & -\frac{I_q}{nC_o} & -\frac{I_o}{nC_o} \end{bmatrix} \tag{42}$$

$$B_{3n} = \begin{bmatrix} -\frac{I_d}{nC_o} & -\frac{I_q}{nC_o} & -\frac{-(n-1)I_o}{nC_o} \end{bmatrix} \tag{43}$$

The photovoltaic field has been modelled by linearization of the current curve of the panels around an operation point close to the maximum power point (MPP). In Equation (44) the linearization of the current supplied by a PV field composed by n_p parallel branches (or strings) and n_s series panels per string is shown, following the procedure that was described in [17]. I_{pv} and V_{pv} are the current and the voltage, respectively, of the PV field at the considered MPP:

$$k_{pv} = -\frac{n_p}{n_s} \cdot \frac{I_{pv}}{V_{pv}}\bigg|_{MPP} \tag{44}$$

The expressions of the variables at the operating point are represented in Table 1. To simplify the calculation of these terms, the mutual coupling terms of the three-phase inductors have been neglected and the capacitors of the filters have been not considered, so that the currents in the grid side of the filters (I_{1dqoi}) and in the converter side (I_{2dqoi}) agree ($I_{dqoi} \approx I_{1dqoi} \approx I_{2dqoi}$). In addition, the expressions of the operating point are obtained by taking into account the control objectives, so that currents in the active channel of each inverter are considered of the same value because an equally distribution of the power generation between the inverters is desired. This condition will be imposed by the control stage. To obtain null reactive power and avoid circulating currents, the reactive and the zero-sequence components of the currents must be null.

Table 1. Simplified expression of the operating point values.

Variable		Variable		Variable	
V_{gd}	V_{gRMS}(phase-phase)	V_{gq}	0	V_{go}	0
I_d	$\frac{V_{pv}I_{pv}}{n \cdot V_{gd}}$	I_q	0	I_o	0
D_d	$\frac{V_{gd}}{V_{pv}}$	D_q	$\frac{\omega I_d \left(L_a + n L_g + L_b \right)}{V_{pv}}$	D_o	0

3. Description of the Proposed Control Architecture for *n* Parallel PV Inverters

3.1. Overview of the Control Stage

Figure 7 shows the proposed control structure for the previosuly described PV system. It is composed of *n* *d*-channel and *n* *q*-channel current control loops (in both cases, one per inverter) and $(n - 1)$ *o*-channel current controllers. It is worth noting that more than one circulating current path exists in the schematic of two parallel inverters. Instead of looking at all individual circulating currents, the zero-sequence current can be used to represent the overall circulating current. The zero-sequence current is defined as the sum of all phases' currents in one inverter. For instance, taken the inverter 1: $i_{o1} = i_{a1} + i_{b1} + i_{c1}$. It is obvious that $i_{o1} = 0$ if only one inverter is connected, because it generates a set of balanced currents ($i_{a1} + i_{b1} + i_{c1} = 0$). Taking *n = 2* (two modules connected in parallel), $i_{o1} = -i_{o2}$, so that both currents can be controlled by acting only on one of them. In general, for *n* inverters in parallel, $n - 1$ controllers are needed to regulate all the *o*-channel currents.

The PV field voltage is controlled by a single outer voltage loop, which calculates the reference signal for the *d*-channel inner controllers. The reference for the voltage loop would be calculated by a Maximum Power Point Tracking (MPPT) algorithm, whose study is beyond the scope of this work. With this approach, the *d*-component of the current allows the control of the active power of the system and the *q*-channel current control loop allows the control of the reactive power. Unity power factor is usually desired to take profit of the full power capacity of inverters to generate active power, so the reference of the *q*-channel control loop is normally zero. Finally, each power module has its own Space Vector Modulator (SVM), which works from the duty cycles calculated by the current controllers.

It is worth to point out that the novelties of the proposed control stage with regard to the conventional one are, basically, two. On one hand, the zero sequence component of three-phase inverters are normally supposed to be zero, so that this component is not controlled. In the proposed solution, the zero sequence components are controlled with a reference signal i_o* = 0 to avoid the appearance of circulating currents among inverters. On the other hand, 2D-SVM are normally used for three-phase three-wire systems. However, 2D-SVM can only operate in the $\alpha\beta$ plane so it can not generate zero sequence components that are outside that plane, as it is the case of the zero-sequence componentes. To overcome this limitation, the use of a 3D-SVM is proposed and detailed in the next section. Note that only $(n - 1)$ 3D modulators are needed, the same number as *o*-channel current controllers.
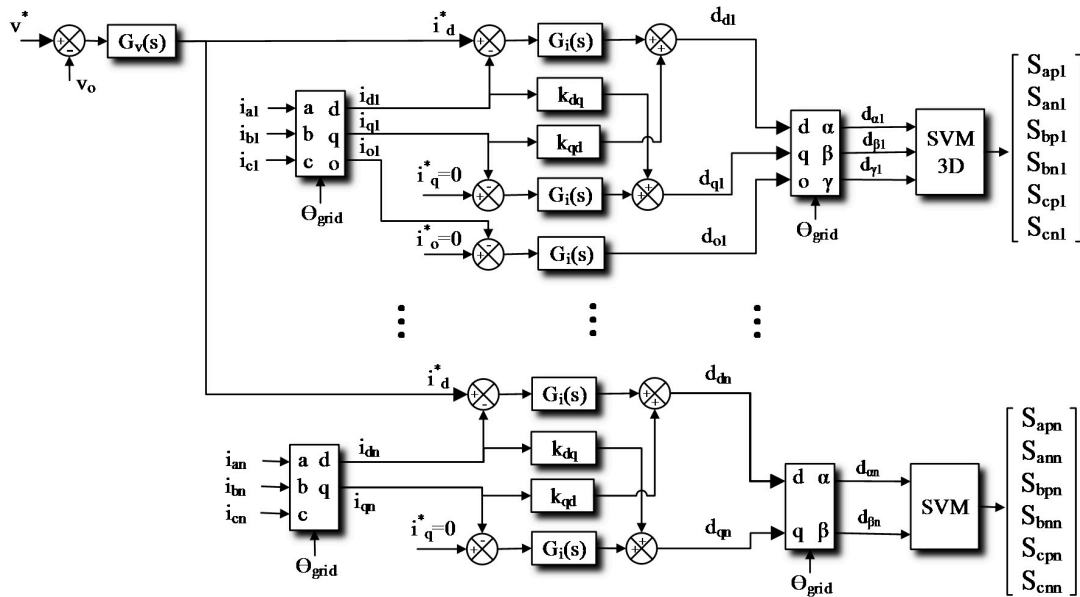
Figure 7. Schematic of the proposed Control Stage.

In any system represented in the synchronous reference frame, there are coupling terms between the *d*- and *q*-axis. The small-signal model presented in Section 2 show the presence of such coupling terms. Equations (47)–(48) express the decoupling terms between both axis, which have been caculated by necglecting the filter capacitors, so that the currents in the grid side of the filters (I_{1dqoi}) and in the converter side (I_{2dqoi}) agree ($I_{dqoi} \approx I_{1dqoi} \approx I_{2dqoi}$). Assuming, in adition, that $\hat{v}_{pv}(s)\hat{v}_{gd}(s) = 0$, it is obtained (45). Being ε_{idi} the current error in the *d*-channel, and *PIi* a proportional-integral regulator, the control action on the *d*-channel is expressed as in Equation (46). From Equations (45)–(46) it is obtained the decoupling term K_{qd}. The K_{dq} term is calculated following the same procedure. These decoupling terms are valid from dc up to medium frequencies:

$$\hat{d}_{di}(s) \cdot V_{pv} + \omega\left(L_a + nL_g + L_b\right) \cdot \hat{i}_{qi}(s) = \left(L_a + nL_g + L_b\right) s \cdot \hat{i}_{di}(s) \tag{45}$$

$$\hat{d}_{di}(s) = PI_i(s)\hat{\varepsilon}_{idi}(s) + K_{qd} \cdot \hat{i}_{qi}(s) \tag{46}$$

$$k_{qd} = -\frac{\omega\left(L_a + nL_g + L_b\right)}{V_{pv}} \tag{47}$$

$$k_{dq} = \frac{\omega\left(L_a + nL_g + L_b\right)}{V_{pv}} \tag{48}$$

Equations (49)–(51) represent the current control loop gains in the *d*- *q*- and *o*-channels, respectively. In the equations, R_s is the current sensor gain, $PI_i(s)$ are proportional-integral regulators and $D(s)$ represents a delay equivalent to one switching period, which has been calculated by means of a second-order Padé approximant. The duty cycle to current transfer functions are obtained from the state space model of the system by means of MATLAB$^{\text{TM}}$ (R2015b). Note that the current sensors are placed on the inverter side of the LCL filter. Locating the sensors on this side of the inverter improves the robustness of the system instead of placing the sensors on the grid side [18]:

$$T_{idi}(s) = R_s \cdot PI_i(s) \cdot D(s) \cdot \frac{\hat{i}_{i1di}(s)}{\hat{d}_{di}(s)} \tag{49}$$

$$T_{iqi}(s) = R_s \cdot PI_i(s) \cdot D(s) \cdot \frac{\hat{i}_{i1qi}(s)}{\hat{d}_{qi}(s)} \tag{50}$$

$$T_{ioi}(s) = R_s \cdot PI_i(s) \cdot D(s) \cdot \frac{\hat{i}_{1loi}(s)}{\hat{d}_{oi}(s)} \tag{51}$$

The voltage control loop gain follows Equation (52). In this equation, β is the voltage sensor gain and $PI_v(s)$ is a proportional-integral regulator:

$$T_{vi}(s) = \beta \cdot PI_v(s) \cdot \frac{\hat{i}_{1di}(s)}{\hat{i}_{dref}(s)} \cdot \frac{\hat{v}_o(s)}{\hat{i}_{1di}(s)} = \beta \cdot PI_v(s) \cdot \frac{\hat{v}_o(s)}{\hat{i}_{dref}(s)} \tag{52}$$

3.2. Three-Dimension Space Vector Modulator

A three-phase converter has eight possible commutation vectors. In Table 2 the phase to neutral voltages of the different switching vectors are expressed taking into account that the low frequency components of the voltage between the middle point of the dc-link and the neutral of the mains are zero, so it can be considered that the neutral point of the grid and the middle point of the dc-link are virtually connected at the frequency of the fundamental line voltage [19].

Table 2. Commutation vectors of 3D-SVM.

v_φ	$v_{0\text{-}000}$	$v_{1\text{-}100}$	$v_{2\text{-}110}$	$v_{3\text{-}010}$	$v_{4\text{-}011}$	$v_{5\text{-}001}$	$v_{6\text{-}101}$	$v_{7\text{-}111}$
v_A	$-\frac{1}{2}V_{pv}$	$\frac{1}{2}V_{pv}$	$\frac{1}{2}V_{pv}$	$-\frac{1}{2}V_{pv}$	$-\frac{1}{2}V_{pv}$	$-\frac{1}{2}V_{pv}$	$\frac{1}{2}V_{pv}$	$\frac{1}{2}V_{pv}$
v_B	$-\frac{1}{2}V_{pv}$	$-\frac{1}{2}V_{pv}$	$\frac{1}{2}V_{pv}$	$\frac{1}{2}V_{pv}$	$\frac{1}{2}V_{pv}$	$-\frac{1}{2}V_{pv}$	$-\frac{1}{2}V_{pv}$	$\frac{1}{2}V_{pv}$
v_C	$-\frac{1}{2}V_{pv}$	$-\frac{1}{2}V_{pv}$	$-\frac{1}{2}V_{pv}$	$-\frac{1}{2}V_{pv}$	$\frac{1}{2}V_{pv}$	$\frac{1}{2}V_{pv}$	$\frac{1}{2}V_{pv}$	$\frac{1}{2}V_{pv}$
v_α	0	$\sqrt{2/3}V_{pv}$	$\frac{1}{\sqrt{6}}V_{pv}$	$-\frac{1}{\sqrt{6}}V_{pv}$	$-\sqrt{2/3}V_{pv}$	$-\frac{1}{\sqrt{6}}V_{pv}$	$\frac{1}{\sqrt{6}}V_{pv}$	0
v_β	0	0	$\frac{1}{\sqrt{2}}V_{pv}$	$\frac{1}{\sqrt{2}}V_{pv}$	0	$-\frac{1}{\sqrt{2}}V_{pv}$	$-\frac{1}{\sqrt{2}}V_{pv}$	0
v_o	$\frac{-\sqrt{3}}{2}V_{pv}$	$\frac{-1}{2\sqrt{3}}V_{pv}$	$\frac{1}{2\sqrt{3}}V_{pv}$	$\frac{-1}{2\sqrt{3}}V_{pv}$	$\frac{1}{2\sqrt{3}}V_{pv}$	$\frac{-1}{2\sqrt{3}}V_{pv}$	$\frac{1}{2\sqrt{3}}V_{pv}$	$\frac{\sqrt{3}}{2}V_{pv}$

Figure 8 represents the switching vectors in $\alpha\beta 0$ (Clarke) coordinates. The switching vectors projected onto the α, β plane define six prisms. Each prism contains two tetrahedrons defined by two non-zero switching consecutive vectors and the neutral vectors v_0 and v_7 alternatively.
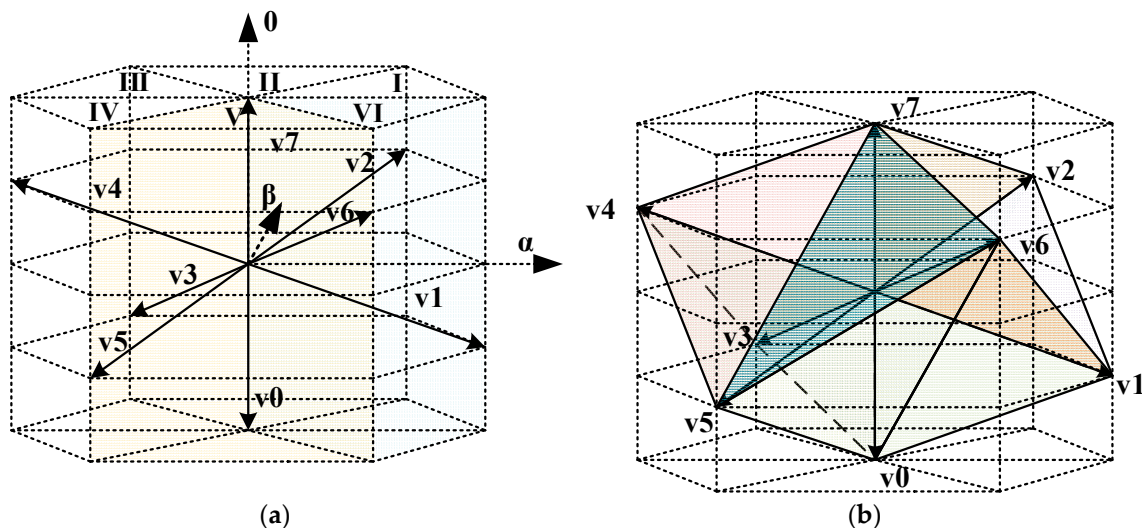

Figure 8. (**a**) Spatial distribution of the commutation vectors; (**b**) Spatial distribution of the tetrahedrons.

The tetrahedron that contains the reference vector must be calculated to obtain the switching vectors that must be applied [20]. It is necessary to calculate the time of application of the vectors, projecting the reference vector to the switching vectors that delimit the tetrahedrons.

Equations (53)–(56) define the time of application of each switching vector. The residual time in every switching period is applied equally to the neutral vector v_0 and v_7:

$$
\begin{bmatrix} d_n \\ d_{n+1} \\ d_0 \end{bmatrix} = \frac{1}{V_{pv}} \begin{bmatrix} v_n & v_{n+1} & v_0 \end{bmatrix}^T
\tag{53}
$$

$$
t_{v_n} = T_s \cdot d_n
\tag{54}
$$

$$
t_{v_{n+1}} = T_s \cdot d_{n+1}
\tag{55}
$$

$$
t_{v_0} = T_s \cdot d_{v_0}
\tag{56}
$$

The distribution time of the commutation vectors follows normally a symmetric distribution. Then, the time of application of each non-neutral vector is distributed in two periods before and after the v_0 vector. It is important to reduce the number of commutations in order to decrease power losses in semiconductors. Table 3 represents the vectors sequence that must be applied in each prism.

Table 3. Commutation vectors sequence in each prism.

Prism	Commutation Vectors Sequence
I	v_7-v_2-v_1-v_0-v_1-v_2-v_7
II	v_7-v_2-v_3-v_0-v_3-v_2-v_0
III	v_7-v_4-v_3-v_0-v_3-v_4-v_7
IV	v_7-v_4-v_5-v_0-v_5-v_4-v_7
V	v_7-v_6-v_5-v_0-v_5-v_6-v_7
VI	v_7-v_6-v_1-v_0-v_1-v_6-v_7

4. Application to a 2 MW PV System Composed by Four 500 kW Modules in Parallel

The proposed control structure has been applied to a 2 MW PV system composed by four modules, each one of 500 kW, as it is shown in Figure 9. In this section, it is presented the MATLAB^{TM} script that has been developed to study the dynamic response of the system. Then, some results are presented to validate the concept.
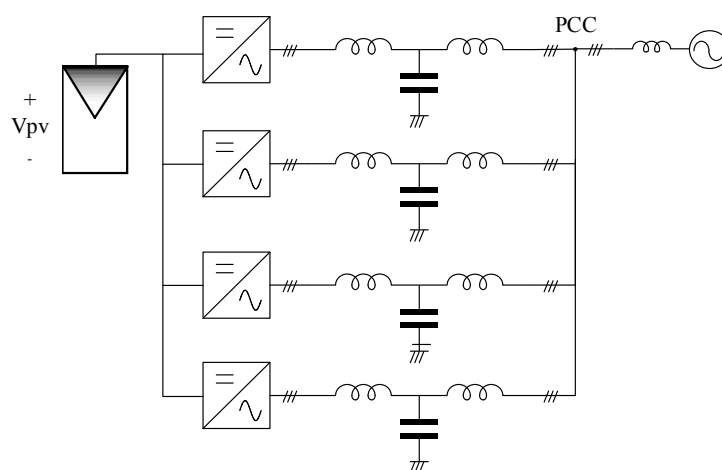

Figure 9. Line diagram of the 2 MW centralized PV inverter under study.

Table 4 indicates the value of the parameters corresponding to one of the inverters under study.

Table 4. Parameters of the Parallel Inverters.

Parameter	Nominal Value	Parameter	Nominal Value
V_g-RMS (line voltage)	230 V	M_a	-20 μH
V_{pv} (MPPT range)	[650–820] V	M_b	-10 μH
V_{dc} max	1000 V	C_f	500 μF
P_n	500 kW	R_d	0.1 Ω
C_o	15 mF	f_{sw}	2 kHz
L_a	80 μH	R_s	1 V/A
L_b	40 μH	β	1 V/V

An issue that is especially relevant for the analysis and design of high power PV inverters is the value of the grid impedances, L_g, which strongly depends on the Point of Common Coupling (PCC) where the PV installation is connected to the grid. To analyze this question, let us define the short-circuit factor R_{sc} as the relation between the short-circuit power S_{sc} at the connection point and the nominal power S_n of the PV system, following Equation (57):

$$R_{sc} = \frac{S_{sc}}{S_n} \tag{57}$$

Assuming that the short-circuit impedance is mainly inductive, the grid inductance (i.e., the short-circuit inductance) L_g can be expressed by Equation (58):

$$L_g \approx \frac{3 \cdot V_g^2}{\omega \cdot R_{sc} S_n} \tag{58}$$

According to R_{sc}, the nature of the grid can be classified as weak (for R_{sc} low) and strong (for R_{sc} high). In the case under study, three values of L_g have been considered to analyze the dynamic response of the PV system with the proposed control stage, as it has been summarized in Table 5.

Table 5. Summary of the considered values for the grid inductance L_g.

Nature of the Grid	R_{sc}	L_g
Weak	5	50 μH
Normal	20	12.7 μH
Strong	100	2.5 μH

4.1. Dynamic Analysis of the Control Loops

In this section it is studied the stability of the control loops of the whole system. The MATLAB$^{\text{TM}}$ script employed to obtain the dynamics of the control loops is presented in Figures 10 and 11. Figure 10 shows the code that allows the study of the state-space model, taking into account the decoupling terms. Figure 11 shows the part of the code that it has been used to calculate the current and voltage control loop gains. Figure 12 illustrates the interconnections that are described in the MATLAB$^{\text{TM}}$ script.

In Figure 10, firstly, the section "parameters definition" describes the parameters of the system under study, as they were expressed in Table 4. Then, the operating point variables and the developed state-space equations are expressed, following Table 1 and (26)–(44), respectively. Note that the matrices A and B are not detailed because their size is excessive to this paper. They must be added to the script following Equations (30)–(31). Then, the "ss" function of MATLAB$^{\text{TM}}$ is employed to generate the state-space model of the system, starting from the A, B, C and D matrices. The obtained state-space model, "G_without_dec", is not decoupled. To add the decoupling terms between the *d*- and *q*-channels that were presented in Equations (47)–(48), a decoupling matrix, "Dec", has been generated. After combining the decoupling matrix and the model of the system by means of a positive "feedback" function, the decoupled state-space model, "G_dec", is obtained. Figure 11 shows the

process to calculate the current and voltage control loop gains. In this part of the code, it is defined a delay equivalent to one switching period, which has been calculated by means of a second-order Padé approximant. After that, it is presented the expression of the proportional-integral current regulators (59) and Equations (49)–(51) are added to the script. Note that the duty cycle to current transfer functions are obtained with the "tf" function of MATLAB. This function generates the transfer function of the selected input, $\hat{d}_{di}, \hat{d}_{qi}, \hat{d}_{oi}$, to output variables, $\hat{i}_{1di}, \hat{i}_{1qi}, \hat{i}_{1oi}$, respectively, starting from the decoupled state-space model of the system "G_dec". Finally, the "margin" command deploys the Bode plot of the respective transfer function, as Figure 13 shows, and calculates the crossover frequency and the gain and the phase margins. Because of the components in each inverter are considered to have the same value, the dynamic response is the same in the *d*-, *q*- and *o*-channel of all inverters. For this reason, only one inverter needs to be studied.

```
%=========================================================================
%Modelling and control of parallel-connected transformerless inverters
%for large photovoltaic farms
%=========================================================================
%M. Liberos, G. González-Medina, G. Garcerá, E. Figueres.
%GSEI. UPV, Valencia, Spain
%-------------------------------------------------------------------------
%Parameters definition
%-------------------------------------------------------------------------
f=50;        w=2*pi*f; s=tf('s');     %Grid frequency/Laplace variable
Vpv=820;                              %MPPT voltage [650...820]
P=2000e3;    n=4;     Co=15e-3;       %Nominal power/n inverters/DC-link
La=80e-6;    Ma=-20e-6;              %LCL filter
Lb=40e-6;    Mb=-10e-6;  Cf=500e-6;  Rd=0.1; %LCL filter
Fsw=2e3;     Ts=1/(2*Fsw);           %fsw
Rs=1;        beta=1;                  %current/voltage sensor gain
Kcc=100;     Lg=400^2/(Kcc*2*pi*f*P);%5_weak 20_normal 100_strong/Grid induc
%-------------------------------------------------------------------------
%Operating point variables and state-space equations
%-------------------------------------------------------------------------
Vgd=400;                Vgq=0;                      Vgo=0;
Id=Vpv*Ipv/(n*Vgd);     Iq=0;                       Io=0;
Dd=Vgd/Vpv;             Dq=w/Vpv*(La+n*Lg+Lb)*Id;   Do=0;
%X=Y=[i1d1,i1q1,i1o1,i2d1,i2q1,i2o1,...i1dn,i1qn,i1on,i2dn,i2qn,i2on,
%     vcd1,vcq1,vco1,...,vcdn,vcqn,vcon,Vpv];
%U=[dd1,dq1,do1,...ddn,dqn,don,Vgd,Vgq,Vgo];
A=[];    B=[];    C=eye(6*n+3*n+1);   D=zeros(6*n+3*n+1,n*3+3);
G_without_dec=ss(A,B,C,D);
%-------------------------------------------------------------------------
%Decoupling terms
%-------------------------------------------------------------------------
Kqd=[0 -w*((La+n*Lg)+Lb)/Vpv];      Kdq=[w*((La+n*Lg)+Lb)/Vpv 0];
Dec=tf([Kqd [0 0] [0 0] [0 0]; Kdq [0 0] [0 0] [0 0];
        [0 0] Kqd [0 0] [0 0]; [0 0] Kdq [0 0] [0 0];
        [0 0] [0 0] Kqd [0 0]; [0 0] [0 0] Kdq [0 0];
        [0 0] [0 0] [0 0] Kqd;[0 0] [0 0] [0 0] Kdq]);
in_Dec=[1 2 4 5 7 8 10 11];     out_Dec=[1 2 7 8 13 14 19 20];
G_dec=feedback(G_without_dec,Dec,in_Dec,out_Dec,+1);
```

Figure 10. MATLAB^{TM} script. Definition of the state-space model.

```
%=======================================================================
%Current control loop gain
%=======================================================================
delay=(1-Ts/2*s+Ts^2/12*s^2)/(1+Ts/2*s+Ts^2/12*s^2);%Delay 2nd order Padé
Kp=0.00025;     Ki=0.1;   PI=tf([Kp Ki],[1 0]);       %PI regulator
Gild1_dd1=tf(G_dec(1,1));        %Tf i2d1/dd1
Tid1=Rs*PI*delay*Gild1_dd1;      %D-channel current control gain
figure (1);     margin (Tid1);
Gilq1_dq1=tf(G_dec(2,2));        %Tf i2q1/dq1
Tiq1=Rs*PI*delay*Gilq1_dq1;      %Q-channel current control gain
figure (2);     margin (Tiq1);
Gilo1_do1=tf(G_dec(3,3));        %Tf i2o1/do1
Tio1=Rs*PI*delay*Gilo1_do1;      %O-channel current control gain
figure (3);     margin (Tio1);
%=======================================================================
%Voltage control loop gain
%=======================================================================
%Close current control loops
PI_M=[PI 0 0;0 PI 0; 0 0 PI];   PI_Mn=[PI 0 0; 0 PI 0; 0 0 1];
PI_MVg=eye(3);
PI_MATRIX=tf([PI_M zeros(3,3) zeros(3,3) zeros(3,3) zeros(3,3);
              zeros(3,3) PI_M zeros(3,3) zeros(3,3) zeros(3,3);
              zeros(3,3) zeros(3,3) PI_M zeros(3,3) zeros(3,3);
              zeros(3,3) zeros(3,3) zeros(3,3) PI_Mn zeros(3,3);
              zeros(3,3) zeros(3,3) zeros(3,3) zeros(3,3) PI_MVg]);
G_PI=series(PI_MATRIX,G_dec);    %Series connection PI and G_dec
K=Rs*eye(n*3-1);                 %Rs Sensor matrix
in_CL_I=[1 2 3 4 5 6 7 8 9 10 11];
out_CL_I=[1 2 3 7 8 9 13 14 15 19 20];
G_CL_I=feedback(G_PI,K,in_CL_I,out_CL_I);

Kpv=20;     Kiv=100;   PIv=tf(-[Kpv Kiv],[1 0]);   %PIv regulator
GVpv_idref1=tf(G_CL_I(n*6+n*3+1,1));      %Fdt Vpv/idref
Tv1=beta*PIv*GVpv_idref1;       %Voltage control loop gain
figure (4);     margin(Tv1);
```

Figure 11. MATLAB^{TM} script. Current and voltage control loop gains.
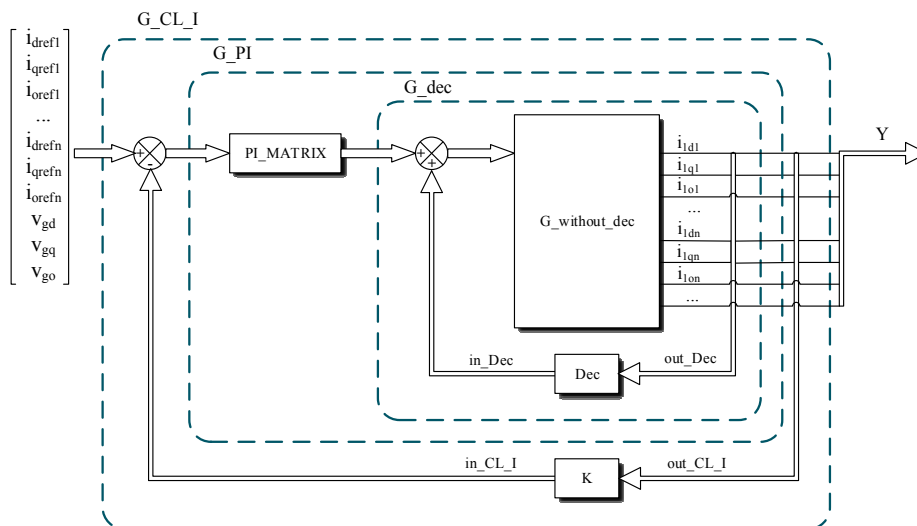

Figure 12. MATLAB^{TM} scheme of interconnection.

Before calculating the voltage control loop gain, the closed current control loops are defined. First, a "PI_MATRIX" containing the expressions of the regulators for the three current loops of each inverter,

is generated and it is connected to the state-space model. Note that this matrix has n d-, n q-, and $n - 1$ o-current regulators expressed as "PI_M" and "PI_Mn". The "PI_MATRIX" is connected in series to the state-space model. There is a value of "1" for the "PI_Mn" and the "PI_MVg" values where a regulator must not be connected to the disturbance inputs, $\hat{d}_{on}$, $\hat{v}_{gd}$, $\hat{v}_{gq}$ and $\hat{v}_{go}$. A sensor current gain matrix, "K", is also created to take into account the gain of the sensors. Then, a negative "feedback" function is used to close the current loops, by linking the duty cycle (inputs) with the sensed currents (outputs), of "G_PI". As a result, it is obtained the model of the system after closing the current loops, "G_CL_I".

Finally, it is obtained the sensed current to voltage transfer function, "GVpv_idref1". Then, the expression of the proportional-integral voltage regulator (Equation (60)) and the one of the voltage current loop gain (Equation (52)) are added. The "margin" command is applied to evaluate the stability of the voltage loop.

The vectors "in_Dec" and "in_CL_I" contains the inputs of "G_without_dec" and "G_PI", respectively, that are involved in the feedback loop. Similarly, "out_Dec" and "out_CL_I" specifies the outputs that are used for feedback. The resulting matrix after applying the "feedback" command, has the same inputs and outputs as the initial system.

It is worth noting that the expressions of the regulators have been chosen by means of an iterative trial and error procedure, using as design criteria the following:

- The crossover frequency of the current loops gain should be much higher than the fundamental frequency of the grid. In addition, it should be much lower than the switching frequency to avoid large-signal instabilities.
- The crossover frequency of the voltage loop should be much lower than the one of the current loops (typically around a factor 1/10).
- In both cases, proper stability margins (PM > 45° and GM > 6 dB) should be obtained.

Equations (59) and (60) express the chosen proportional-integral regulators for the current control loops and for the voltage control loop, respectively. As it will be shown later, the dynamics of the three current loops (d, q and o) are similar, so their corresponding controllers can have the same expression:

$$PI_i(s) = 0.00025 + \frac{0.1}{s} \tag{59}$$

$$PI_v(s) = -20 - \frac{100}{s} \tag{60}$$

Figure 13 represents the Bode plots (dB, deg) of the three current loop gains, $T_{id}(jw)$ (49), $T_{iq}(jw)$ (50) and $T_{io}(jw)$ (51) for one of the power modules. Figure 13 also shows the Bode plots of the voltage loop gain, $T_v(jw)$ (52). In all cases, it has been considered that the PV voltage can vary inside the MPPT range (from 650 V to 820 V). In addition, three representative values of the grid inductance have been considered, following Table 5, to take the nature of the grid into account. As can be seen in Figure 13, the dynamics of the system are sensitive to the considered variations of V_{pv} and L_g, but the stability is guaranteed in all cases. Concretely, the crossover frequency of the current loops ranges from 90 Hz to 300 Hz, having a phase margin PM = 50 and a gain margin GM = 5 db in the worst case. Regarding the voltage loop gain, the crossover frequency ranges from 22 Hz to 27 Hz and the phase margin is higher than 90 degrees.
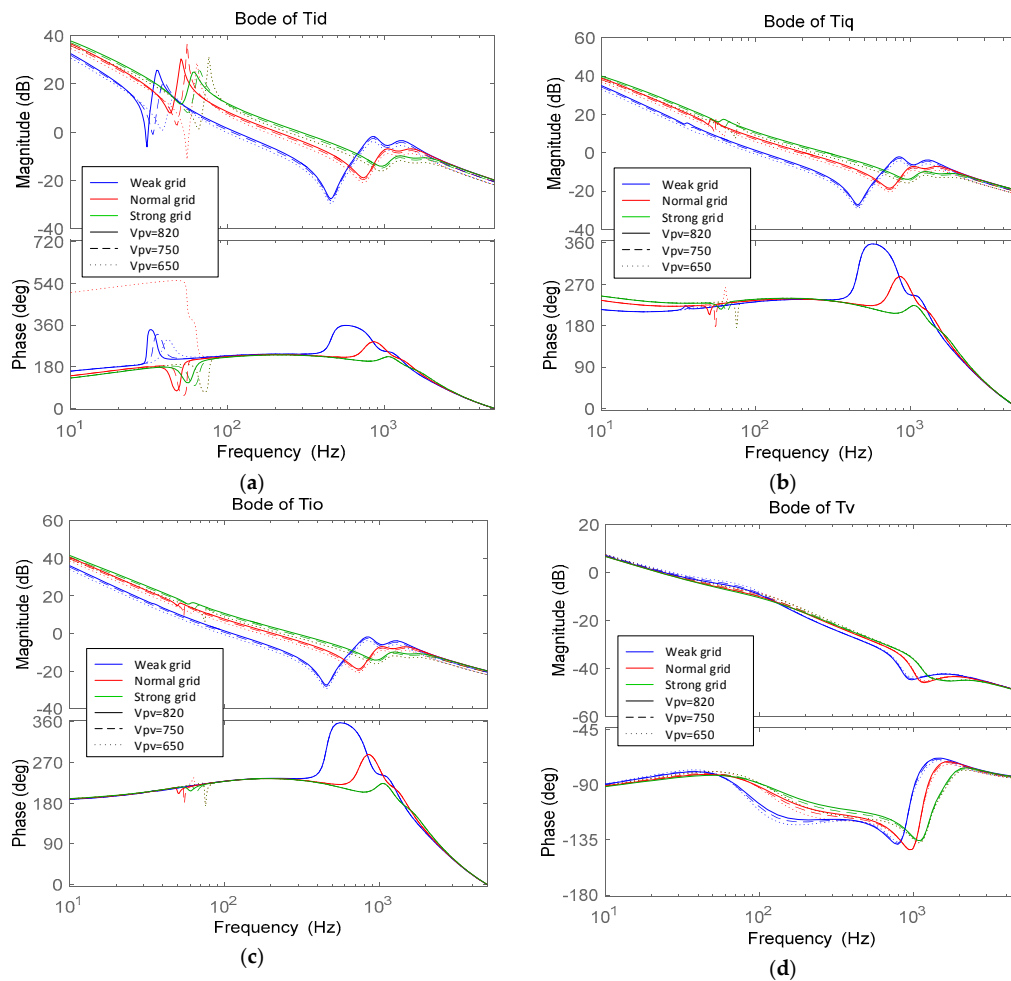
Figure 13. Control loops: (**a**) Current control loop gain in *d*-channel; (**b**) Current control loop gain in *q*-channel; (**c**) Current control loop gain in o-channel; (**d**) Voltage control loop gain.

4.2. Results

To validate the small-signal design in the large signal sense, the performance of the PV system has been evaluated by means of PSIM$^{\text{TM}}$ (10.0) software. Figure 14b shows the evolution of the current (phase *a)* of the four power modules connected in parallel, as the generated power ranges from zero to 1 MW, Figure 14a, and working with a conventional control scheme that doesn't control the zero-sequence components of the currents. It is worth noting that it is desired an equal power distribution among the modules as they connect to the system. In the Introduction (Figure 3), it was explained that this sequence of connection allows having a good efficiency in all the range of power, reducing considerably the power loss when the generated power is low. Figure 14c depicts the zero-sequence current of the inverters. Before the activation of the second inverter, when the first one is managing all the generated power, there is no circulating current. However, after the activation of the second inverter a circulating current appears between both inverters. The same occurs after the activation of the inverters 3 and 4.
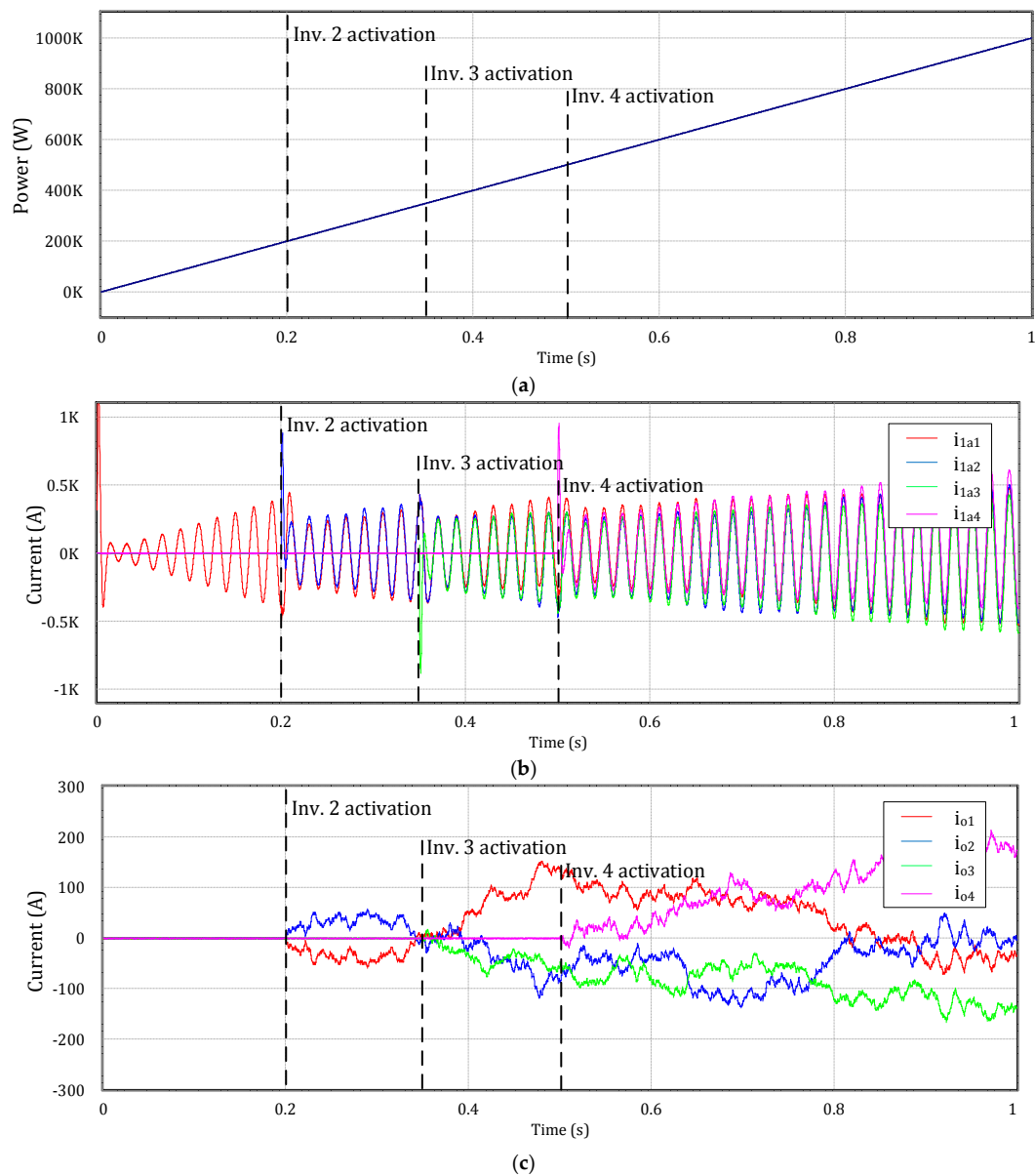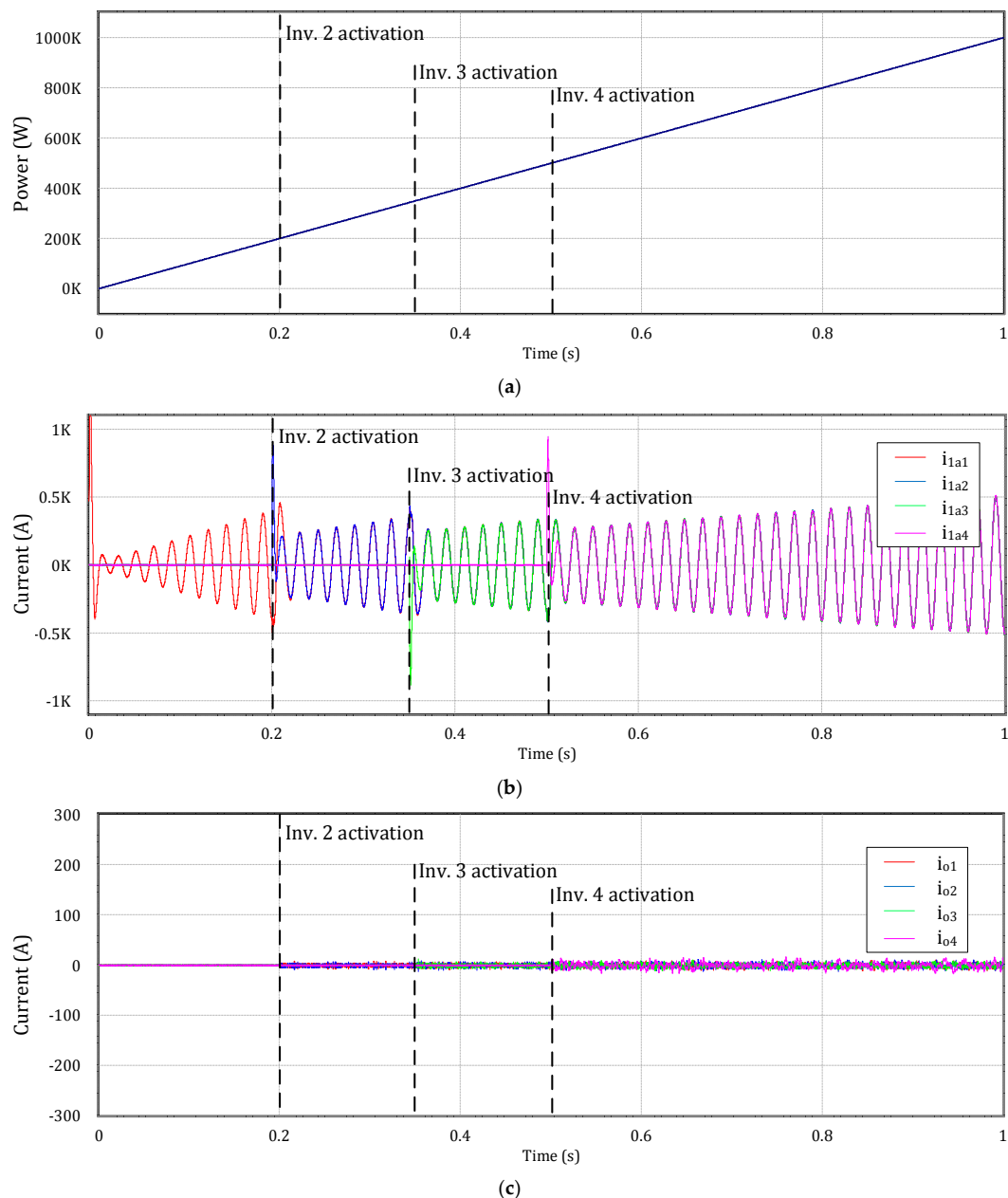
Figure 14. Activation sequence of the inverters without zero-sequence control: (**a**) Generated PV power; (**b**) Current grid in the phase A of each inverter; (**c**) Zero-sequence current of each inverter.

Figure 15 shows the same waveforms, following the same activation sequence of inverters that in Figure 14, but working with the proposed control scheme. It can be seen in Figure 15c that the zero-sequence currents are null, so there are not circulating currents among inverters. It is worth noting that the power distribution among the modules is much better with the proposed control technique.

(a)

(b)

(c)

Figure 15. Activation sequence of the inverters with zero-sequence control: (**a**) Generated PV power; (**b**) Grid current in the phase A of each inverter; (**c**) Zero-sequence current of each inverter.

Figure 16a shows the inverters' currents in steady state and full load conditions. Before the activation of the zero-sequence controllers, there is a significant imbalance between the currents of the inverters and after the activation at $t = 2.4$ s the currents become equal. In this figure it has not been implemented the current limitation of the inverters, so that the generated power is maintained at 2 MW, but some of the modules are overloaded while others are underloaded. Figure 16c depicts the zero-sequence current in each inverter also before and after the activation of the zero-sequence control at $t = 2.4$ s. The circulating current reaches approximately 30% of the fundamental current in the worst case before the activation of the control and then becomes zero.

In practice, the inverters will deliver as maximum their nominal current, so the actual power that could be injected to the grid would be lower. As a result, the power capacity of the PV system would be degraded. This fact is illustrated by Figure 17. In this figure, the performance of the PV system

has been evaluated in similar conditions that in Figure 16, but limiting the inverters' current to their nominal value. Note that, before the activation of the proposed control technique, the PV system can't reach the nominal power. Once the zero sequence controllers are activated, the circulating current disappears and the delivered power is equally distributed among inverters, so the nominal 2 MW can be supplied.
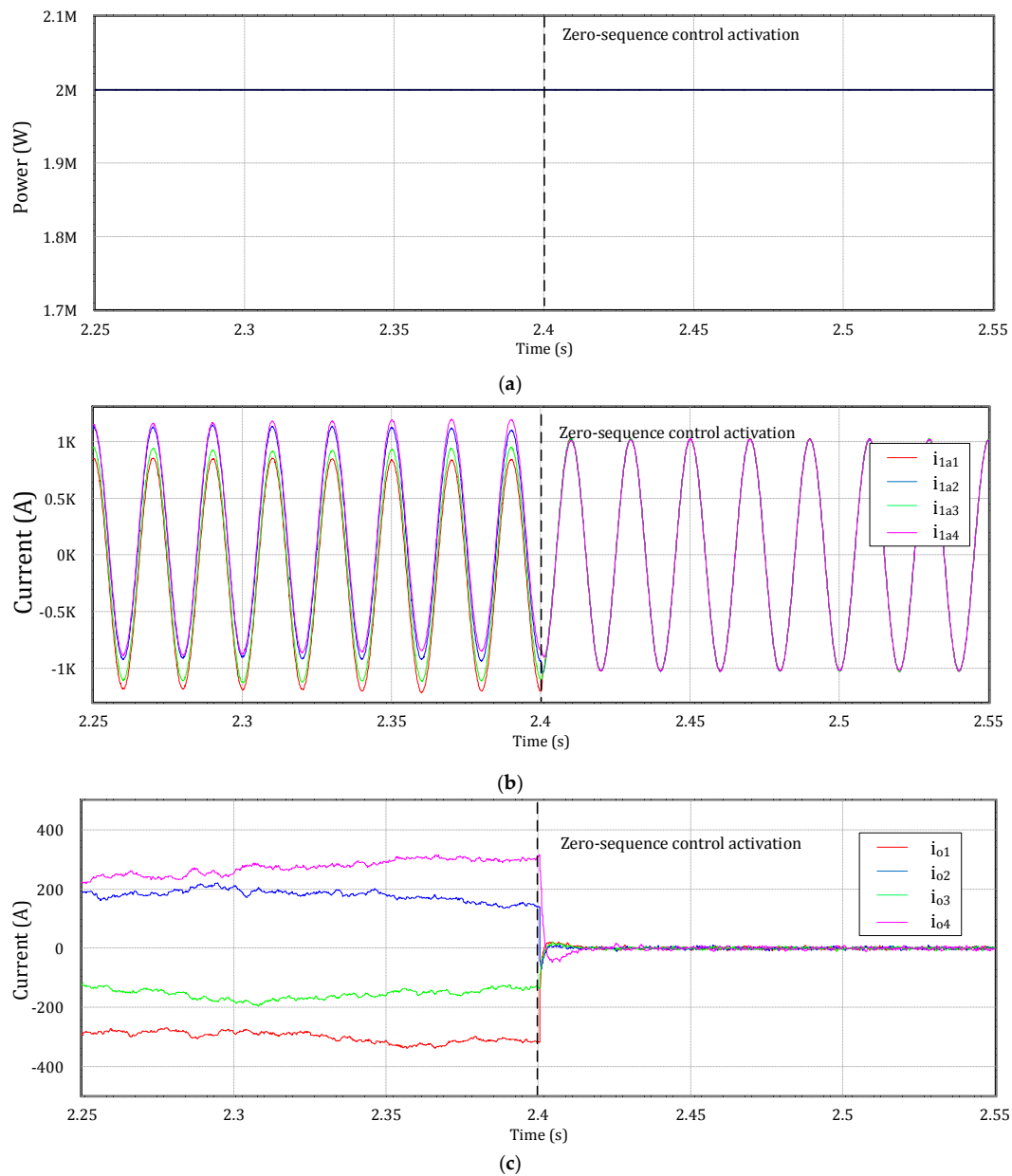

Figure 16. Activation of the zero-sequence control without current limitation: (**a**) Generated PV power; (**b**) Grid current in the phase A of each inverter; (**c**) Zero-sequence current or circulating current of each inverter.
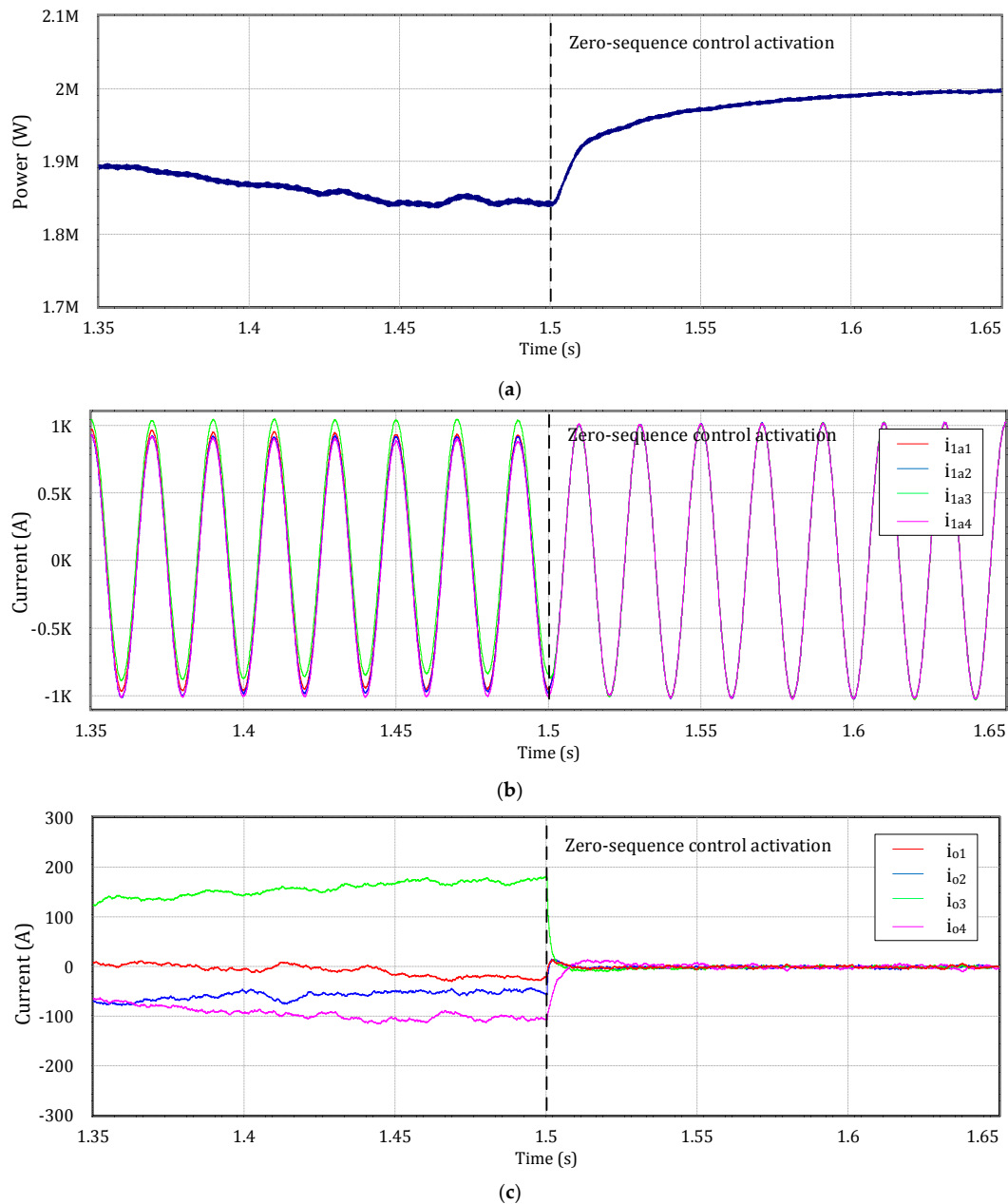
Figure 17. Activation of the zero-sequence control with current limitation: (**a**) Generated PV power (**b**) Grid current in the phase A of each inverter; (**c**) Zero-sequence current or circulating current of each inverter.

5. Conclusions

This work has presented an accurate model of centralized PV transformerless inverters for high power photovoltaic fields composed by *n* parallel modules. Such a power architecture has many benefits such as modularity, good efficiency from low to high power generation and reduced weight, volume and costs. However, it has been outlined that significant circulating currents appear among the modules and this degrades the performance of the PV system.

To overcome this problem, a control technique that regulates the zero-sequence component of the inverters' currents has been proposed. Moreover, it has been pointed that 3D Space Vector Modulators are needed to control the zero-sequence components of the currents.

The proposed control stage has been applied to a 2 MW photovoltaic system composed by four parallel inverters, 500 kW each, that are connected in parallel. The presented results show that, as expected, the circulating currents become zero after activating the control of the zero-sequence component of the inverters' currents. The concept can be easily implemented in PV systems because it does not add significant extra complexity.

Author Contributions: Marian Liberos, Emilio Figueres and Gabriel Garcerá have been developed the main idea, the model and the control of the system; Marian Liberos and Raúl González-Medina have been programming the PSIM^TM simulations; Marian Liberos, Emilio Figueres and Gabriel Garcerá have written the paper.

Conflicts of Interest: The authors declare no conflict of interest. The founding sponsors had no role in the design of the study; in the collection, analyses, or interpretation of data; in the writing of the manuscript, and in the decision to publish the results.

References

1. Pazheri, F.R.; Othman, M.F.; Malik, N.H. A review on global renewable electricity scenario. *Renew. Sustain. Energy Rev.* **2014**, *31*, 835–845. [CrossRef]
2. Subudhi, B.; Pradhan, R. A Comparative Study on Maximum Power Point Tracking Techniques for Photovoltaic Power Systems. *IEEE Trans. Sustain. Energy* **2013**, *4*, 89–98. [CrossRef]
3. Borrega, M.; Marroyo, L.; González, R.; Balda, J.; Agorreta, J.L. Modeling and Control of a Master–Slave PV Inverter With N-Paralleled Inverters and Three-Phase Three-Limb Inductors. *IEEE Trans. Power Electron.* **2013**, *28*, 2842–2855. [CrossRef]
4. Duman, T.; Marti, S.; Moonem, M.A.; Kader, A.A.R.A.; Krishnaswami, H. A Modular Multilevel Converter with Power Mismatch Control for Grid-Connected Photovoltaic Systems. *Energies* **2017**, *10*, 698. [CrossRef]
5. Araujo, S.V.; Zacharias, P.; Mallwitz, R. Highly Efficient Single-Phase Transformerless Inverters for Grid-Connected Photovoltaic Systems. *IEEE Trans. Ind. Electron.* **2009**, *57*, 3118–3128. [CrossRef]
6. Satcon, Pv Inverters. PowerGate Plus 500 kW. Available online: http://www.satcon.com (accessed on 18 August 2017).
7. Agorreta, J.L.; Borrega, M.; López, J.; Marroyo, L. Modeling and Control of N-Paralleled Grid-Connected Inverters With LCL Filter Coupled Due to Grid Impedance in PV Plants. *IEEE Trans. Power Electron.* **2010**, *26*, 770–785. [CrossRef]
8. Power Electronics. Available online: http://www.power-electronics.com (accessed on 18 August 2017).
9. ABB, ABB Central Inverters. PVS980—1818 to 2091 kVA. Available online: http://new.abb.com (accessed on 18 August 2017).
10. Infineon, Central Inverter Solutions. Available online: https://www.infineon.com/cms/en/applications/solar-energy-systems/central-inverter-solutions/ (accessed on 18 August 2017).
11. Xiao, H.F.; Xie, X.J.; Chen, Y.; Huang, R.H. An optimized transformerless Photovoltaic Grid-Connected Inverter. *IEEE Trans. Ind. Electron.* **2011**, *58*, 1887–1895. [CrossRef]
12. Ye, Z.; Boroyevich, D.; Lee, F. Modeling and control of zero-sequence current in parallel multi-phase converters. In Proceedings of the Power Electronics Specialists Conference, Galway, Ireland, 23–23 June 2000.
13. Mazumder, S.M. A novel discrete control strategy for independent stabilization of parallel three-phase boost converters by combining space-vector modulation with variable-structure control. *IEEE Trans. Power Electron.* **2003**, *18*, 1070–1083. [CrossRef]
14. Pan, C.T.; Liao, Y.H. Modeling and Control of Circulating Currents for Parallel Three-Phase Boost Rectifiers With Different Load Sharing. *IEEE Trans. Ind. Electron.* **2008**, *55*, 2776–2785.
15. Ogasawara, S.; Takagaki, J.; Akagi, H.; Nabae, A. A novel control scheme of a parallel current-controlled PWM inverter. *IEEE Trans. Ind. Appl.* **1992**, *28*, 1023–1030. [CrossRef]
16. Ye, Z.H.; Boroyevich, D.; Choi, J.Y.; Lee, F.C. Control of circulating current in two parallel three-phase boost rectifiers. *IEEE Trans. Power Electron.* **2002**, *2*, 609–615.

17. Figueres, E.; Garcera, G.; Sandia, J.; Gonzalez-Espin, F.; Rubio, J.C. Sensitivity Study of the Dynamics of Three-Phase Photovoltaic Inverters With an LCL Grid Filter. *IEEE Trans. Ind. Electron.* **2009**, *56*, 56–706. [CrossRef]

18. Figueres, E.; Garcera, G.; Sandia, J.; Gonzalez-Espin, F.; Calvo, J.; Vales, M. Dynamic Analysis of Three-phase Photovoltaic Inverters with a High Order Grid Filter. In Proceedings of the IEEE International Symposium on Industrial Electronics, Vigo, Spain, 4–7 June 2007.

19. Mohd, A.; Ortjohann, E.; Hamsic, N.; Sinsukthavorn, W.; Lingemann, M.; Schmelter, A.; Morton, D. Control strategy and space vector modulation for three-leg four-wire voltage source inverters under unbalanced load conditions. *IET Power Electron.* **2010**, *3*, 323–333. [CrossRef]

20. Albatran, S.; Fu, Y.; Albanna, A.; Schrader, R.; Mazzola, M. Hybrid 2D-3D Space Vector Modulation Voltage Control Algorithm for Three Phase Inverters. *IEEE Trans. Sustain. Energy* **2013**, *4*, 734–744. [CrossRef]